



Topological paramagnetic excitons of localized f electrons on the honeycomb lattice

Alireza Akbari , Burkhard Schmidt , and Peter Thalmeier
Max Planck Institute for the Chemical Physics of Solids, 01187 Dresden, Germany



(Received 24 March 2023; revised 14 June 2023; accepted 14 July 2023; published 27 July 2023)

We investigate the dispersive paramagnetic excitons on the honeycomb lattice that originate from the crystalline electric field split localized f -electron states in the *paramagnetic* state due to intersite exchange. We start with a symmetry analysis of possible Ising-type singlet-singlet and xy -type singlet-doublet models. The former supports only symmetric intersite exchange while the latter additionally allows for antisymmetric Dzyaloshinski-Moriya exchange interactions. We calculate the closed expressions for magnetic exciton dispersion using both response function formalism and bosonic Bogoliubov approach. We do this for the most general model that shows inversion-symmetry breaking on the honeycomb lattice but also discuss interesting special cases. By calculating Berry curvatures and Chern numbers of paramagnetic excitons we show that the xy model supports nontrivial topological states in a wide range of parameters. This leads to the existence of excitonic topological edge states with Dirac dispersion lying in the zone boundary gap without the presence of magnetic order.

DOI: [10.1103/PhysRevB.108.045143](https://doi.org/10.1103/PhysRevB.108.045143)

I. INTRODUCTION

Localized $4f$ and $5f$ electron states are organized in terms and multiplets according to Hund's rules. Since the spin-orbit coupling is generally larger than crystalline electric field (CEF) potentials acting on the f electrons the total angular momentum of multiplets is a good quantum number. The perturbation of the CEF at the f -electrons site which originates from the surrounding ligands splits the ground-state J multiplet into a series of CEF multiplets with degeneracies corresponding to the possible representations of the f -site symmetry. This is conveniently described within Steven's operator technique used in Refs. [1,2] with an effective parametrized CEF Hamiltonian restricted to the lowest J -multiplet subspace (Appendix A). The parameters may be formally expressed in terms of a point-charge model (PCM) with screened ligand charges, however, in practice they are usually determined from experiment. The sizes of the splittings depend much on the material but are generally, at least for a subset of CEF multiplets, in the thermal range and lead to a large variety of physical effects [3,4] for accessible temperatures. In particular the temperature dependence of the susceptibility over the whole range of CEF splitting allows to extract model sets of parameters for the CEF potential, which is, however, rarely unique.

For intermetallic compounds the conduction electrons (c) have an effective onsite exchange interaction J_{cf} with CEF states (obtained from eliminating the cf hybridization and

f - f Coulomb interaction [5]). First, it will lead to a broadening of CEF excitations [6] observable in inelastic neutron scattering (INS). If the CEF ground state is degenerate, a low-temperature Kondo effect results in coherent heavy-fermion behavior often accompanied by unconventional superconductivity [7]. Furthermore, the elimination of J_{cf} leads to effective unretarded intersite exchange interactions of the Ruderman-Kittel-Kasuya-Yoshida (RKKY) type which for degenerate CEF ground state may cause magnetic order according to the Doniach phase diagram [5]. But even in the paramagnetic state their presence entails the formation of collective magnetic exciton modes which can be viewed as propagating localized CEF excitations between the multiplets. These magnetic exciton modes have been found in numerous $4f$ compounds using INS [3,6]. Determining the dispersion and intensity of magnetic excitons such experiments also allow to identify suitable model Hamiltonians for the coupled CEF states by deriving multiplet splittings and intersite exchange-coupling models from comparison with theoretical results for the model [8,9]. The latter are most conveniently obtained with the RPA response function formalism of the dynamic magnetic susceptibility [3] which we will also partly use in this work.

Of particular interest are CEF systems with singlet non-magnetic ground state as occurs for f -electron materials with integer J , e.g., Pr and U compounds ($J = 4$). These cannot exhibit magnetic order of the conventional quasiclassical type by aligning preexisting moments as in the case of degenerate magnetic CEF ground state. Rather the creation of local moments and their ordering appears simultaneously through quantum mechanical mixing of excited CEF states into the singlet ground state, e.g., in two-singlet [10,11] and three-singlet [12] CEF level systems caused by intersite exchange. This happens only when the latter is sufficiently large as expressed by a dimensionless control parameter ξ (Sec. III A). If it is smaller than a critical value or negligible the compound stays paramagnetic [13].

Published by the American Physical Society under the terms of the Creative Commons Attribution 4.0 International license. Further distribution of this work must maintain attribution to the author(s) and the published article's title, journal citation, and DOI. Open access publication funded by the Max Planck Society.

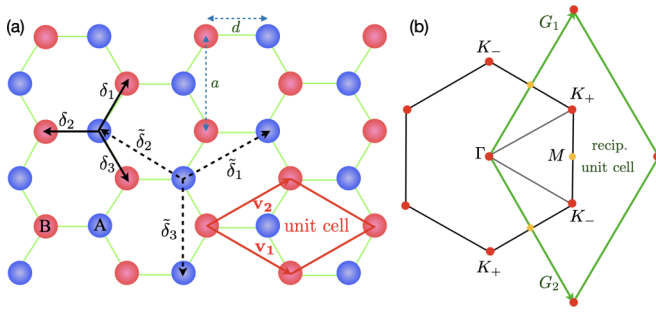


FIG. 1. (a) Honeycomb lattice structure (triangular sublattices $\sigma = A, B$) with unit cell (primitive lattice vectors $\mathbf{v}_{1,2}$), first-neighbor vectors δ_i ($i = 1 - 3, z = 3$), and second-neighbor vectors $\pm\tilde{\delta}_i$ ($i = 1 - 3, z = 6$) indicated. The corresponding symmetric exchange constants are I_σ and I_σ^z , respectively. Lattice constant denoted by a and $d = a/\sqrt{3}$ is the first-neighbor distance. The DM exchange couplings between second neighbors at $\tilde{\delta}_i, -\tilde{\delta}_i$ are $-D_i^z, D_i^z$, respectively. The distance between the zigzag chains (e.g., along y direction) is given by $x_0 = \frac{\sqrt{3}}{2}$. (b) Reciprocal lattice with primitive unit cell and associated vectors $\mathbf{G}_1, \mathbf{G}_2$. The inequivalent zone boundary valleys are indicated by $\mathbf{K}_+, \mathbf{K}_-$. The expressions for the vectors in direct and reciprocal space are given in Appendix D.

Such type of singlet ground-state-induced moment magnetism is preceded in the paramagnetic phase by a strong temperature dependence and a softening of a critical magnetic exciton mode to a varying degree at the ordering wave vector. This type of induced singlet-singlet magnetic order is found, e.g., in Pr metal (under pressure) [3,14,15] and Pr compounds like PrSb [16] and Pr₃Tl [8,17], PrCu₂ [18], PrNi [19], and also in TbSb [20] and various U compounds [21–23]. In the Pr systems the large hyperfine interaction with nuclear moments can also play an essential role in the ordering [3].

The mechanism of induced order is not restricted to dipolar magnetism, for example, in YbRu₂Ge₂ the lowest $J = \frac{7}{2}$ Kramers doublets form a quartet that supports induced quadrupolar order due to nondiagonal quadrupole matrix elements [24,25] between them.

In these materials it is frequently possible to restrict model calculations to a reduced low-energy level scheme consisting just of the singlet ground state and an excited multiplet (e.g., singlet or doublet) and ignoring the higher-lying CEF states. Such simplified models will be also used in this work. They allow closed analytic solutions for the exciton bands and a detailed investigation how their structure and properties depend on the model parameters. Here we investigate the magnetic excitons for such simplified singlet ground-state systems in the paramagnetic state where the f -electron sites are forming a two-dimensional (2D) honeycomb lattice. It has a two-atom basis (A, B) (Fig. 1), each of them belonging to a trigonal Bravais lattice with site symmetry C_{3v} . The honeycomb lattice may be realized as a planar structure within a three-dimensional (3D) lattice. This structure is relevant for various f -electron compounds like Na₂PrO₃ [26], TmNi₃Al₉ [27], and recently a new class of promising $4f$ (RE = Tm, Ho) honeycomb materials BaRE₂(SiO₄)₆ has been discovered [28]. All compounds mentioned have integer total angular momentum J . For concreteness we focus on $J = 4$ realized in trivalent Pr($4f^2$) and possibly U($5f^2$) magnetic

ions but may also be applicable to trivalent Tb and Tm with $J = 6$ and Ho with $J = 8$.

We begin with an appropriate motivation why this is an interesting problem. It is already well known that in the ferromagnetically (FM) or antiferromagnetically (AFM) ordered honeycomb lattice magnon bands may become topologically nontrivial and support magnonic edge modes within the gap of split 2D bulk magnon modes [29–35]. This well-developed subject is reviewed in Refs. [36–40]. The nontrivial topology in 2D is characterized by a nonzero Chern number of the bulk bands which is the integral over the Berry curvature obtained from the magnon bands and their eigenstates. The gap opening between the two magnon bands (due to sublattice structure) is a prerequisite for nonvanishing Chern number. It can only be achieved if an antisymmetric Dzyaloshinskii-Moriya (DM) spin-exchange term between nearest neighbors (NN) is included. Any symmetric exchange (between first neighbors on A, B or between further neighbors) will preserve the degeneracy of magnon bands at zone boundary points of the trigonal Brillouin zone (BZ) leading to Chern number zero. The DM interaction is allowed because the centers of NN A - B are not inversion centers of the lattice, only the centers of hexagons and next-nearest-neighbor (NNN) bonds (Fig. 1). The DM interaction thus enables nonzero Chern number and consequently (nondegenerate) magnon edge states inside the bulk gap. They can carry a transverse heat current, thus leading to a topological thermal magnon Hall and Nernst effect discussed in theoretical investigations, e.g., Refs. [30,41] and found experimentally in a similar kagome lattice FM [42].

In this work we will study the *paramagnetic excitons* on the honeycomb lattice with nonmagnetic singlet ground-state f electrons on the C_{3v} sites having in mind the potentially interesting topological properties in analogy to the magnonic case. The aim of this work is twofold.

First, we want to give a complete theory of magnetic excitons in the paramagnetic state for CEF split f electrons on the honeycomb lattice comprising two trigonal sublattices A, B and C_{3v} site symmetry based on the reduced level schemes. We focus on two representative cases for C_{3v} CEF states: An Ising-type singlet-singlet system and an xy -type singlet-doublet level scheme. Thereby we make the most general assumption that inversion symmetry is broken leading to inequivalent CEF splitting and interaction parameters for sublattices A, B . The aim of this part is to give a solid theoretical foundation for inelastic neutron scattering (INS) experiments on singlet ground-state honeycomb f -electron paramagnets. We will derive general model expressions for dispersions and intensities that may be used to analyze such experiments provided a restriction to one excited singlet or doublet can be justified, as is frequently the case in Pr and U compounds.

Characteristically, the magnetic excitons appear already in the paramagnetic phase of singlet ground-state systems as opposed to magnons which are seen only in the ordered phase as collective excitations of the order parameter resulting from a degenerate magnetic ground state and thus they are clearly separate types of magnetic excitations. In an INS experiment both magnetic excitons and magnons can be distinguished in a standard way from phonon excitations of the underlying lattice by following their intensity as function of total momentum transfer $\tilde{\mathbf{k}}$ (including the reciprocal lattice vector).

In the former the intensity decreases with $\tilde{\mathbf{k}}$ due to the magnetic f -electron form factors while in the latter it increases quadratically with $\tilde{\mathbf{k}}$ [6]. The magnetic excitons considered here bear some formal similarity to the zero-field dispersive triplon excitations of spin dimer compounds between singlet and excited triplet states of the dimer [43]. The dispersion is caused by interdimer exchange smaller than the dimer singlet-triplet gap. However, such suitably sized dimerization is not relevant in any of the above-mentioned compounds and also not in the honeycomb lattice discussed here with only equidistant f -electron sites.

The Ising-type model is convenient for demonstrating the two techniques of calculating the magnetic exciton modes, namely, the RPA response function and bosonic Bogoliubov quasiparticle techniques. We will show that indeed they give equivalent results. Applied to the Ising case we calculate the dispersion and intensity of the two modes symmetrically split by the intersublattice interactions and an additional contribution resulting from the intrasublattice terms. For equivalent sublattices the modes will be degenerate at specific zone boundary points \mathbf{K}_{\pm} and we demonstrate how they will be split when inversion-symmetry breaking occurs.

Using the same techniques we investigate the richer singlet-doublet xy -type model. Because of nonzero diagonal matrix elements for both J_x, J_y total angular momentum components an asymmetric DM interaction is possible for the intrasublattice exchange. Due to the doublet degeneracy four magnetic exciton modes exist in principle. For equivalent sublattices they consist of a pair of twofold-degenerate modes which can develop a gap at the \mathbf{K}_{\pm} zone boundary due to the presence of the DM interaction. A further splitting into four modes occurs when the sublattices become inequivalent. This theory is sufficiently general to be used for modeling INS experiments for all possible singlet-singlet and singlet-doublet CEF systems on compounds with f electrons located on the honeycomb lattice.

Second, we show that in the xy -type model the DM term may lead to interesting nontrivial topology of the magnetic exciton bands. We stress that this happens in the *paramagnetic* state of f electrons on the honeycomb lattice. It is our primary intention to demonstrate that magnetic order is not a prerequisite for the existence of topological magnetic excitations and corresponding edge modes. For this purpose we investigate the behavior of Berry curvature and associated Chern numbers of paramagnetic exciton bands and discuss their model parameter dependence. We show that as function of the size of inversion-symmetry breaking transitions from zero to integer Chern numbers are possible. In the latter case we also derive the existence of the boundary magnetic exciton modes in a continuum approximation around the Dirac points \mathbf{K}_{\pm} . Finally we discuss that in contrast to topological magnons in a FM the paramagnetic topological magnetic excitons do not lead to a thermal Hall effect as is indeed required by the absence of time-reversal symmetry breaking.

In Sec. II we give a brief introduction to f -electron CEF states in less common C_{3v} symmetry with details relegated to Appendix A. Then Sec. III discusses the Ising-type models in various techniques and the principle of induced magnetic order. In Sec. IV the xy -type model, its characteristic four

dispersion branches, and their topological properties including edge modes are investigated. Section VI discusses some numerical results and finally Sec. VII gives the summary and conclusion.

II. CEF STATES ON THE HONEYCOMB LATTICE, SINGLET-SINGLET, AND SINGLET-DOUBLET MODELS

The point-group symmetry for the sites on the 2D honeycomb lattice with two basis atoms (A, B) is C_{3v} , composed of threefold rotations and reflections on perpendicular planes 120° apart (Fig. 1). The A, B sublattice sites have no inversion symmetry in C_{3v} . The honeycomb space group $P6/mcc$, however, contains the inversion with centers given by the midpoint of bonds and the center of hexagons. The point-group symmetry leads to a CEF potential (restricted to the lowest J multiplet) given as a sum of Stevens operators $O_n^m(\mathbf{J})$ ($m \leq n \leq 6$) (see detailed analysis in Appendix A).

In this work we are interested exclusively in f -electron shells with integer J to have the possibility of a nonmagnetic singlet CEF ground state $|0\rangle$ with $\langle 0|\mathbf{J}|0\rangle = 0$. Among the trivalent rare-earth (RE) ions this is possible for $J = 4$ (Pr), $J = 6$ (Tb, Tm), and $J = 8$ (Ho). We will restrict to the simplest case of $J = 4$. The complete characterization of CEF energies and states in C_{3v} symmetry is given in Appendix A. In this group the $J = 4$ space decomposes into irreducible representations $2\Gamma_1 \oplus \Gamma_2 \oplus 3\Gamma_3$, i.e., three singlets ($\Gamma_1^{a,b}, \Gamma_2$) and three doublets ($\Gamma_3^{a,b,c}$) which are linear combinations of free-ion states $|J, M\rangle$ ($|M| \leq J$). The two $\Gamma_1^{a,b}$ singlets are characterized by one (θ) and the three $\Gamma_3^{a,b,c}$ doublets by generally three (χ, ϕ, α) mixing angles determined by the set of CEF parameters B_n^m in Eq. (A1) while the unique Γ_2 is fully determined by C_{3v} symmetry. Explicitly, the full orthonormal CEF state basis is given in Appendix A. Here we list only the singlets and one representative doublet Γ_3^a necessary for the following analysis:

$$\begin{aligned}
 |\Gamma_{1a}\rangle &= \cos\theta|4, 0\rangle + \frac{1}{\sqrt{2}}\sin\theta(|4, 3\rangle - |4, -3\rangle), \\
 |\Gamma_{1b}\rangle &= -\sin\theta|4, 0\rangle + \frac{1}{\sqrt{2}}\cos\theta(|4, 3\rangle - |4, -3\rangle), \\
 |\Gamma_2\rangle &= \frac{1}{\sqrt{2}}(|4, 3\rangle + |4, -3\rangle), \\
 |\Gamma_{3a}^{\pm}\rangle &= \sin\chi(\cos\phi|4, \pm 4\rangle + \sin\phi|4, \mp 2\rangle) \\
 &\quad \pm \cos\chi|4, \pm 1\rangle.
 \end{aligned} \tag{1}$$

The CEF energies E_{Γ} of these eigenstates are complicated combinations of the B_n^m (Appendix A). Because there are six independent parameters and six irreducible representations the energy levels can in principle take any ordering.

For investigating the magnetic exciton modes it is important to calculate the dipolar matrix elements between the CEF states. The J_{α} ($\alpha = x, y, z$) operators connect states with $M' = M, M \pm 1$. Here we restrict to two important cases discussed in detail in the following: The singlet-singlet $\Gamma_{1a,b}-\Gamma_2$ subspaces and the singlet-doublet $\Gamma_2-\Gamma_{3a}$ subspaces. Their

dipolar matrix elements are given by

$$\begin{aligned} \langle \Gamma_2 | J_z | \Gamma_1 \rangle &= m, \\ \langle \Gamma_2 | J_x | \Gamma_3^\pm \rangle &= \tilde{m}/\sqrt{2}, \quad \langle \Gamma_2 | J_y | \Gamma_3^\pm \rangle = \pm i\tilde{m}/\sqrt{2}, \end{aligned} \quad (2)$$

where we defined $m = 3 \sin \theta$ or $m = 3 \cos \theta$ for $\Gamma_{1a,b}$ singlets, respectively, and $\tilde{m} = (1/\sqrt{2}) \sin \chi [\sqrt{7} \sin \phi + 2 \cos \phi]$ for Γ_{3a} . The matrix elements of J_x, J_y between the $\Gamma_{1a,b}$ - Γ_2 subspaces vanish as well as those within Γ_{3a} doublet subspace. Therefore, the singlet-singlet Γ_1 - Γ_2 model is of the Ising type while the singlet-doublet model Γ_2 - Γ_3 is of the xy type for the inelastic CEF excitations. The latter would also be realized in a Γ_1 - Γ_3 type model. These selection rules follow also directly from the group multiplication table [44] of C_{3v} considering the fact that J_z transforms like Γ_2 and (J_x, J_y) transform like Γ_3 . We note that nondiagonal quadrupolar matrix elements between ground and excited states are only allowed for the xy -type model. Quadrupolar intersite interaction terms will not be included here as they contribute only indirectly to the dipolar dynamic response functions of INS in zero field [45].

To devise suitably general models for both cases in the following sections we start from two basic observations on the honeycomb structure: First, the center of second-neighbor bonds (A - A , B - B) is not an inversion center. Therefore, in addition to symmetric exchange asymmetric Dzyaloshinski-Moriya (DM) exchange between second neighbors (dashed lines in Fig. 1) may be present. Second, although the bond centers of first neighbors are inversion centers meaning that A, B sublattices are equivalent, this can be removed when the 2D honeycomb lattice is placed into a 3D crystal where the chemical environment of the basis atoms A, B between the honeycomb layers may be different. This could be achieved by sandwiching the f -electron honeycomb layer between nonmagnetic honeycomb layers with different chemical occupations of A, B known, e.g., from unconventional honeycomb superconductors [46]. Using such 3D layered structure with local inversion-symmetry breaking on the f -honeycomb sites their CEF potentials (multiplet splittings) and interactions on the A, B sublattices may also be generally different. This possibility should be incorporated in both models. It means that inversion symmetry with respect to center of first-neighbor A - B bonds and hexagon centers is also broken. We stress that such full 2D inversion-symmetry breaking in honeycomb models has already been proposed and investigated before for the FM-ordered honeycomb lattice [32].

III. SINGLET-SINGLET ISING-TYPE MODEL

First we address the more simple and instructive case of the singlet-singlet CEF model. Our calculations of exciton modes will be based on RPA response function theory as well as Bogoliubov transformation approach. The former can also be applied at finite temperatures while the latter allows to address topological properties of the modes due to a bosonic representation used for the local CEF excitations.

For concreteness we assume Γ_2 to be the ground state and one of the $\Gamma_{1a,b}$ the excited state, and the inverted scheme leads to identical results. Furthermore, we do not distinguish between a and b representations and denote by $m = m_a, m_b$

any of the two matrix elements between ground and excited states. The singlet-singlet CEF Hamiltonian is then given by

$$H = \sum_{\Gamma\sigma i} E_{\Gamma\sigma}^\sigma |\Gamma\sigma i\rangle \langle \Gamma\sigma i| - I \sum_{\langle ij \rangle} J_{iA}^z J_{jB}^z - \sum_{\langle\langle ij \rangle\rangle\sigma} I_2^\sigma J_{i\sigma}^z J_{j\sigma}^z. \quad (3)$$

Here $\sigma = A, B$ denotes the two sublattices and i, j the first-neighbor lattice sites on each of them and $\Gamma = \Gamma_2, \Gamma_1$ the two singlet states. In the first term the CEF energies $E_{\Gamma\sigma}$ (and the $\Gamma_{1a,b}$ excited states) may depend on the sublattices A, B and similar for the exchange terms. We fix $E_{\Gamma_2}^\sigma = 0$ on each and denote the relative excited state energy by $\Delta_\sigma = E_{\Gamma_1\sigma}$ (we suppress the a, b index of both possible $\Gamma_{1a,b}$ representations from now on). The second and third terms describe the symmetric exchange *between* A and B sublattices (first neighbors) and *within* A and B sublattices (second neighbors), respectively. Having in mind intermetallic f -electron compounds the effective intersite exchange terms may be generated by the virtual exchange of, e.g., $5d$ and $6s$ conduction electron-hole excitations [47,48]. Note that in the above model only J_z has nonzero matrix elements [Eq. (2)]. Therefore, it is of the Ising type and in particular no DM exchange is supported because this needs at least two components of \mathbf{J} to have nonzero matrix elements (Sec. IV).

A. Response functions and magnetic exciton modes

The interaction terms in Hamiltonian of Eq. (3) allow the $\Gamma_2 \leftrightarrow \Gamma_1$ excitations of the paramagnetic state to propagate from site to site and thus acquire a dispersion. They are commonly designated “magnetic excitons” to distinguish them from magnons which require a *magnetically ordered* ground state with broken time-reversal symmetry. The most convenient way to obtain the dispersion of magnetic excitons is the calculation of the dynamic magnetic susceptibility $\hat{\chi}(\mathbf{q}, i\omega_n)$ in RPA. It is given by the 2×2 sublattice-space matrix

$$\hat{\chi}(\mathbf{k}, i\omega_n) = [1 - \hat{I}(\mathbf{k})\hat{u}(i\omega_n)]^{-1}\hat{u}(i\omega_n), \quad (4)$$

where

$$\hat{u}(i\omega_n) = \begin{pmatrix} u_A(i\omega_n) & 0 \\ 0 & u_B(i\omega_n) \end{pmatrix} \quad (5)$$

and

$$\hat{I}(\mathbf{k}) = \begin{pmatrix} z_2 I_2^A \gamma_2(\mathbf{k}) & z I \gamma(\mathbf{k}) \\ z I \gamma^*(\mathbf{k}) & z_2 I_2^B \gamma_2(\mathbf{k}) \end{pmatrix} \quad (6)$$

are the single-ion susceptibility and exchange matrices, respectively. In the latter $z = 3$ and $z_2 = 6$ are first- and second-neighbor coordination numbers and $\gamma(\mathbf{k}), \gamma_2(\mathbf{k})$ the corresponding structure functions of the honeycomb lattice [Eq. (E2)]. We note that the above exchange model for the 2D honeycomb can easily be generalized to a 3D stacked arrangement by introducing additional interlayer exchange constants and appropriately modified 3D structure functions. The exchange functions (25) for the xy -type model may be generalized in a similar fashion.

Furthermore, in the singlet-singlet model we have ($\sigma = A, B$)

$$u_\sigma(i\omega_n) = \frac{2m_\sigma^2 \Delta_\sigma P_\sigma(T)}{\Delta_\sigma^2 - (i\omega_n)^2}. \quad (7)$$

The temperature-dependent factor $P_\sigma(T) = \tanh \frac{\Delta_\sigma}{2T}$ in the numerator is equal to the difference of thermal occupations of ground and excited singlet states and Δ_σ and m_σ are the (generally different) singlet-singlet splitting and matrix elements. The magnetic exciton bands [there are two ($\kappa = \pm$) due to the A and B sublattices] are then obtained as the collective modes, i.e., the singularities of the dynamic susceptibility as determined by $\det \hat{\chi}(\mathbf{k}, i\omega_n) = 0$. Solving this equation a closed expression for the magnetic exciton dispersions $\omega_\kappa(\mathbf{k})$ may be evaluated:

$$\omega_\pm^2(\mathbf{k}) = \frac{1}{2}[\omega_A^2(\mathbf{k}) + \omega_B^2(\mathbf{k})] \pm \left[\frac{1}{4}[\omega_A^2(\mathbf{k}) - \omega_B^2(\mathbf{k})]^2 + 4m_A^2 m_B^2 \Delta_A \Delta_B P_A P_B |I_N(\mathbf{k})|^2 \right]^{\frac{1}{2}},$$

$$\omega_\sigma^2(\mathbf{k}) = \Delta_\sigma [\Delta_\sigma - 2m_\sigma^2 P_\sigma I_D^\sigma(\mathbf{k})]. \quad (8)$$

Here we use the abbreviations $I_D^\sigma(\mathbf{k}) = (z_2 I_2^\sigma) \gamma_2(\mathbf{k})$ and $I_N(\mathbf{k}) = (z_1) \gamma(\mathbf{k})$ for diagonal (D) and nondiagonal (N) intrasublattice and intersublattice exchange in Eq. (6), respectively. Furthermore, the $\omega_{A,B}(\mathbf{k})$ may be interpreted as the separate mode dispersions on $\sigma = A, B$ sublattices when the nearest-neighbor intersublattice coupling $I_N(\mathbf{k})$ is set to zero. Explicitly this formula may also be written as

$$\omega_\pm^2(\mathbf{k}) = \frac{1}{2}(\Delta_A^2 + \Delta_B^2) - [m_A^2 \Delta_A P_A I_D^A(\mathbf{k}) + m_B^2 \Delta_B P_B I_D^B(\mathbf{k})] \pm \left\{ \left[\frac{1}{2}(\Delta_A^2 - \Delta_B^2) - [m_A^2 \Delta_A P_A I_D^A(\mathbf{k}) - m_B^2 \Delta_B P_B I_D^B(\mathbf{k})] \right]^2 + 4m_A^2 m_B^2 \Delta_A \Delta_B P_A P_B |I_N(\mathbf{k})|^2 \right\}^{\frac{1}{2}}. \quad (9)$$

For numerical calculations it is convenient to use three model parameters (dimension energy) $v_s = (m_A m_B I)$ and $v_\sigma^2 = (m_\sigma^2 I_\sigma^2)$ and likewise $|I_N(\mathbf{k})| = m_A m_B |I_N(\mathbf{k})| = (z_1 v_s) \gamma(\mathbf{k})$ and $I_D^\sigma(\mathbf{k}) = m_\sigma^2 I_D^\sigma(\mathbf{k}) = (z_2 v_\sigma^2) \gamma_2(\mathbf{k})$ (see also Appendix B). At low temperatures $T/\Delta_\sigma \ll 1$ we may replace $P_\sigma(T) \rightarrow 1$. The dispersion simplifies further if the intrasublattice exchange $I_D^\sigma(\mathbf{k})$ is absent. Then we get

$$\omega_\pm^2(\mathbf{k}) = \frac{1}{2}(\Delta_A^2 + \Delta_B^2) \pm \left[\frac{1}{4}(\Delta_A^2 - \Delta_B^2)^2 + 4m_A^2 m_B^2 \Delta_A \Delta_B P_A P_B |I_N(\mathbf{k})|^2 \right]^{\frac{1}{2}}. \quad (10)$$

On the other hand, if both first- and second-neighbor exchange are kept but the two sublattice sites are assumed equivalent with $\Delta_A = \Delta_B = \Delta$ and likewise $I_D^A = I_D^B = I_D$ Eq. (9) reduces to

$$\omega_\pm^2(\mathbf{k}) = \Delta \left[\Delta - 2m^2 [I_D(\mathbf{k}) \mp |I_N(\mathbf{k})|] \tanh \frac{\Delta}{2T} \right]. \quad (11)$$

Here the mode splitting of $\omega_\kappa(\mathbf{k})$ can be seen to be directly associated with the intersublattice coupling. The splitting vanishes at the \mathbf{K}_\pm zone boundary points in this special case. In the general case described by Eq. (9) the criterion for

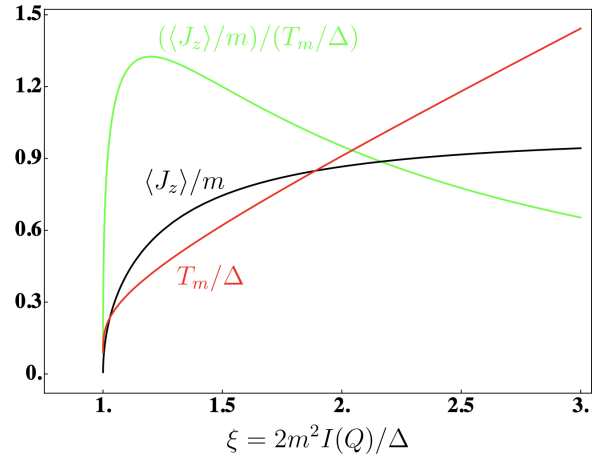


FIG. 2. Ising-type model induced order characteristics signified by control-parameter ξ dependence of ground-state moment $\langle J_z \rangle$ (normalized to m), magnetic ordering temperature T_m (normalized to CEF splitting Δ), and their ratio (see also Ref. [23]).

opening a gap at \mathbf{K}_\pm may be identified as (i) for $\Delta_A \neq \Delta_B$ the gap is always present and (ii) for $\Delta_A = \Delta_B$ one then must have $I_2^A \neq I_2^B$ for the intrasublattice exchange. Furthermore, we can see from the above special case that the bandwidth of magnetic excitons is controlled by the size and \mathbf{k} dependence of exchange interactions, increasing with their strength. It is frequently comparable to the CEF splitting Δ [19,49].

Eventually if the interactions become strong enough the lower mode, e.g., $\omega_-(\mathbf{k})$, may become soft at specific, generally incommensurate wave vector $\mathbf{k}=\mathbf{Q}$ and this heralds a spontaneous induced magnetic order with modulation wave vector \mathbf{Q} of the singlet-singlet system although both CEF singlets are nonmagnetic with $\langle \Gamma_\alpha | J_z | \Gamma_\alpha \rangle = 0$ ($\alpha = 1, 2$). In the above equivalent sublattice case this occurs when the control parameter

$$\xi = \frac{2m^2 I(\mathbf{Q})}{\Delta} > 1, \quad (12)$$

where $I(\mathbf{Q}) = I_D(\mathbf{Q}) + |I_N(\mathbf{Q})|$ is the total exchange Fourier transform. For $\xi > 1$ the transition temperature T_m to the induced moment phase and the size of the induced moment $M_{\mathbf{Q}} = \langle J_z \rangle$ (in units of μ_B) along z are given by [21]

$$T_m \simeq \frac{\Delta}{2 \tanh^{-1}(\frac{1}{\xi})} \simeq \frac{\Delta}{|\ln \xi'|}, \quad (13)$$

$$M_{\mathbf{Q}}/m = \frac{1}{\xi} (\xi^2 - 1)^{\frac{1}{2}} \simeq (2\xi')^{\frac{1}{2}},$$

where the approximate expressions hold close to the critical control parameter, i.e., $\xi \simeq 1 + \xi'$ with $\xi' \ll 1$. Both quantities increase with infinite slope above $\xi = 1$ (Fig. 2). This Ising-type two-singlet induced moment system has also been generalized for the frequently occurring three-singlet model in low-symmetry $4f$ and $5f$ materials [12]. In the present case when the incipient soft mode ($\xi < 1$) appears at $\mathbf{Q} = \mathbf{K}_\pm$ zone boundary positions as is the case in Fig. 3 the magnetic order for critical $\xi = 1$ would correspond to a 120° commensurate spiral structure on each triangular sublattice A, B coupled

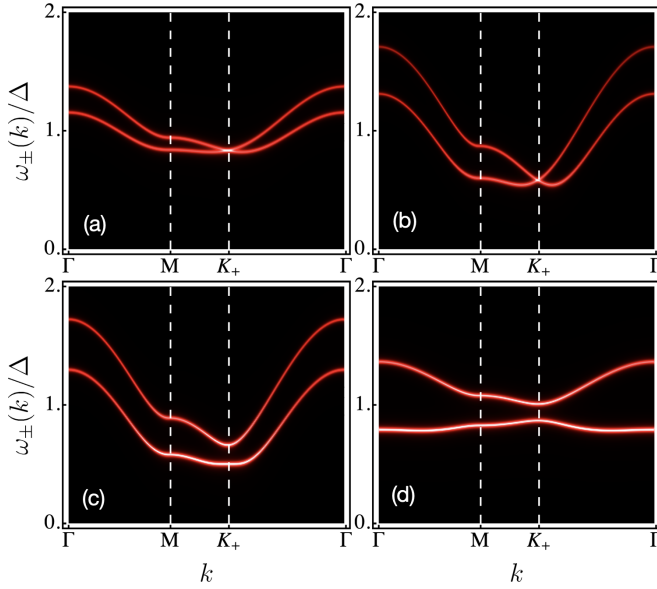


FIG. 3. Typical cases of the Ising model magnetic exciton dispersions. (a) High-temperature case $T = 1.0$ with equal $\Delta_{A,B} = 1$, $v_2^{A,B} = -0.11$, and $v_s = -0.10$ shows moderate dispersion. (b) Same parameters but low-temperature case exhibits large dispersion due to increased thermal population difference of Γ_2, Γ_1 levels. Because of A, B equivalent interaction constants K_+ (and also K_-) is a Dirac point with degenerate and linearly dispersive exciton modes. The splitting of modes for all other \mathbf{k} values is due to intersublattice interaction $I_N(\mathbf{k}) \sim v_s$. (c) $T = 0.1$ case now with distinct $\Delta_{A,B} = \Delta(1 \pm \epsilon)$ where $\Delta = 1$, and $\epsilon = 0.07$ and other constants as in (a) and (b). Now the degeneracy at K_{\pm} is removed. This case shows incipient soft-mode behavior around K_+ indicating closeness to commensurate spiral order. (d) Same case but small $v_2^{A,B} = -0.02$ which reduces the overall dispersion.

ferromagnetically or antiferromagnetically depending on the sign of intersublattice coupling I in Eq. (3).

In this work, however, we restrict the investigation to the *paramagnetic* phase for both CEF models. In the response function formalism it is also straightforward to calculate the momentum and temperature dependence of the intensity of paramagnetic exciton modes that are essential for the interpretation of INS data. It is given by the dynamical structure function

$$S(\mathbf{k}, \omega) = \frac{1}{\pi} [\text{Im} \hat{\chi}_{AA}(\mathbf{k}, \omega) + \text{Im} \hat{\chi}_{BB}(\mathbf{k}, \omega)]. \quad (14)$$

This may be evaluated as

$$\begin{aligned} S(\mathbf{k}, \omega > 0) &= \sum_{\kappa=\pm} I_{\kappa}(\mathbf{k}) \delta(\omega - \omega_{\kappa}(\mathbf{k})), \\ I_{+}(\mathbf{k}) &= \frac{\sum_{\sigma=A,B} m_{\sigma}^2 \Delta_{\sigma} P_{\sigma} (\omega_{+}^2 - \omega_{\sigma}^2)}{\omega_{+}(\mathbf{k}) [\omega_{+}^2(\mathbf{k}) - \omega_{-}^2(\mathbf{k})]}, \\ I_{-}(\mathbf{k}) &= \frac{\sum_{\sigma=A,B} m_{\sigma}^2 \Delta_{\sigma} P_{\sigma} (\omega_{-}^2 - \omega_{\sigma}^2)}{\omega_{-}(\mathbf{k}) [\omega_{+}^2(\mathbf{k}) - \omega_{-}^2(\mathbf{k})]}, \end{aligned} \quad (15)$$

with

$$\begin{aligned} \omega_{+}^2(\mathbf{k}) - \omega_{-}^2(\mathbf{k}) &= 2 \left[\frac{1}{4} (\Delta_A^2 - \Delta_B^2)^2 + 4m_A^2 m_B^2 \Delta_A \Delta_B |I_N(\mathbf{k})|^2 \right]^{\frac{1}{2}}, \end{aligned} \quad (16)$$

where $\bar{\sigma} = B, A$ for $\sigma = A, B$. Here $I_{\kappa}(\mathbf{k})$ denotes the bare intensity of each mode in the INS scattering without Bose, polarization, and atomic form factors [3]; it will be discussed at the end of Sec. III B. We note that in the RPA method and also in the bosonic Bogoliubov approach below the exciton modes are sharp. They may develop a finite broadening or lifetime due to intrinsic exciton-exciton interactions [3,50] or by an extrinsic process originating from the coupling to the electron-hole continuum of (e.g., 5d- and 6s-type) conduction bands as discussed in detail in Ref. [3]. Away from the soft-mode regime the large exciton gap protects them from overdamping by these processes. However, close to the temperature T_m of induced order the softening of $\omega_{-}(\mathbf{Q})$ causes a strong increase of damping channels may lead to a broadening of the mode into a quasielastic line at the ordering wave vector [20]. It should be noted that the relation between mode softening and transition to induced order is generally more complicated than predicted by the RPA approach [3].

B. Bosonic representation of interacting CEF excitations

An alternative approach to the magnetic exciton problem is provided by a bosonic representation of the Hamiltonian and a subsequent application of Bogoliubov technique for diagonalization [51]. It has the advantage of not only providing the dispersion but also the eigenvectors or Bloch states of magnetic exciton modes. On the other hand, it can only be used as a temperature low compared to the CEF splitting. We first apply it for the simple singlet-singlet system, restricting for simplicity to first-neighbor interactions, in order to use it as a guidance for the more complicated singlet-doublet system.

In the restricted Γ_2 - Γ_1 space, considering Eq. (2) we may replace the angular momentum component J_z by sublattice bosonic operators according to

$$J_{iA}^z = m_A (a_i^{\dagger} + a_i), \quad J_{iB}^z = m_B (b_i^{\dagger} + b_i), \quad (17)$$

where the a_i, b_i and $a_i^{\dagger}, b_i^{\dagger}$ satisfy the usual bosonic commutation rules. This replacement produces the proper matrix elements but is restricted to low T because of the different commutation rules and statistics [3,15,51,52]. (The thermal occupation of a finite set of CEF states is determined by their Boltzmann factors while the mapping to bosons creates an enlarged space with arbitrary number of excited bosons leading to bosonic statistics.) Introducing Fourier transforms like $a_{\mathbf{k}} = (1/\sqrt{N}) \sum_i \exp(i\mathbf{k}\mathbf{R}_i) a_i$, etc., and rearranging terms in the first-neighbor exchange Hamiltonian in Eq. (3) we arrive at

$$\hat{H} = \frac{1}{2} \sum_{\mathbf{k}} \phi_{\mathbf{k}}^{\dagger} \hat{h}_{\mathbf{k}} \phi_{\mathbf{k}} + E_0 \quad \text{with} \quad \phi_{\mathbf{k}} = (a_{\mathbf{k}}, b_{\mathbf{k}}, a_{-\mathbf{k}}^{\dagger}, b_{-\mathbf{k}}^{\dagger})^T, \quad (18)$$

where $E_0 = (N/2)(\Delta_A + \Delta_B)$. The components of this four-spinor satisfy the bosonic commutation relations $[\phi_n(\mathbf{k}), \phi_m^{\dagger}(\mathbf{k}')] = \Sigma_z^{nm} \delta_{\mathbf{k}\mathbf{k}'}$ where $\Sigma_z = \tau_z \otimes 1_2 = \text{diag}(1_2,$

-1_2) is composed of the 2×2 unit 1_2 . In this representation we can express

$$\hat{h}_{\mathbf{k}} = \begin{pmatrix} \Delta_A & -\bar{I}_N^*(\mathbf{k}) & 0 & -\bar{I}_N^*(\mathbf{k}) \\ -\bar{I}_N(\mathbf{k}) & \Delta_B & -\bar{I}_N(\mathbf{k}) & 0 \\ 0 & -\bar{I}_N(-\mathbf{k}) & \Delta_A & -\bar{I}_N(-\mathbf{k}) \\ -\bar{I}_N^*(-\mathbf{k}) & 0 & -\bar{I}_N^*(-\mathbf{k}) & \Delta_B \end{pmatrix}, \quad (19)$$

where we used $\bar{I}_N(\mathbf{k}) = (m_A m_B) I_N(\mathbf{k}) = (z v_s) \gamma_{\mathbf{k}}$ which satisfies $\bar{I}_N(-\mathbf{k}) = \bar{I}_N(\mathbf{k})^*$ [Eq. (E2)]. The magnetic exciton modes may be obtained by a paraunitary Bogoliubov transformation. The dispersions are then obtained as eigenvalues obtained from the secular equation $|\Sigma_z \hat{h}_{\mathbf{k}} - \omega| = 0$. The solution of this equation leads to the $T = 0$ exciton modes

$$\omega_{\pm}^2(\mathbf{k}) = \frac{1}{2}(\Delta_A^2 + \Delta_B^2) \pm \left[\frac{1}{4}(\Delta_A^2 - \Delta_B^2)^2 + 4m_A^2 m_B^2 \Delta_A \Delta_B |I_N(\mathbf{k})|^2 \right]^{\frac{1}{2}}. \quad (20)$$

The above Eq. (20) is identical to the RPA result for zero temperature ($P_A = P_B = 1$) obtained before in Eq. (10). Therefore, on the RPA level one may say that temperature enters in the theory just as a parametric change of the effective exchange coupling by modification of the matrix elements to effective ones with the replacement $m_{\sigma}^2 \rightarrow P_{\sigma}(T)m_{\sigma}^2$. In the case of equivalent sublattices A, B the above equation reproduces the $T = 0$ case of Eq. (11). The Bloch functions corresponding to magnetic exciton bands are the eigenvectors of $\Sigma_z \hat{h}_{\mathbf{k}}$ corresponding to the four eigenvalues $\pm \omega_{\pm}(\mathbf{k})$.

At this point, to obtain a preliminary impression of the behavior of magnetic excitons in the honeycomb lattice we discuss the results for the Ising-type model as presented in Fig. 3. In Figs. 3(a) and 3(b) the symmetric case $\Delta_A = \Delta_B$ is shown for elevated (a) and low temperature (b). In the former a moderate dispersion due to small thermal population differences $P_{A,B}$ in Eq. (9) or (11) exists which becomes larger in the low-temperature case. The dispersion of modes is controlled by both by intrasublattice (v_2) and intersublattice (v_s) interaction strength while the mode splitting is only due to the latter (for $v_2^{\sigma} = v_2$). At the \mathbf{K}_{\pm} zone boundary points, however, they become degenerate because $\gamma(\mathbf{K}_{\pm}) = 0$ (Appendix D). This degeneracy is lifted by introducing inequivalent A, B CEF splittings as demonstrated in Figs. 3(c) and 3(d) for two cases with different strength of intrasublattice coupling v_2 . A similar removal of degeneracy at \mathbf{K}_{\pm} occurs if the splittings are kept equal but the intrasublattice couplings $v_2^{A,B}$ become inequivalent. The intensity of the modes corresponds to the brightness of the dispersion curves in Fig. 3. In particular, in Fig. (3 c) one can see that the low-energy modes have larger intensity (are brighter) than the high-energy modes. This is due to the mode frequencies appearing in the denominator of intensity expressions in Eq. (15).

Experimentally the magnetic exciton dispersion curves are determined by INS [8,9,49,53]. Comparison with theoretically predicted model dispersions as derived here [Eqs. (9) and (27)] are the most direct way to extract the physical relevant parameters such as CEF splittings and exchange interaction

strengths of the singlet ground-state honeycomb material investigated.

The consistent results of two different techniques in this section encourage us to consider the more involved and richer singlet-doublet xy -type model. It may also be treated within the response function approach by a simple extension (Appendix D). It has the drawback of giving only the spectral density of the magnetic excitons but not the composition of the eigenmodes which is important for discussing topological properties relevant in the xy model. Therefore, in this case we employ the bosonic technique in the following.

IV. SINGLET-DOUBLET xy -TYPE MODEL

We outline the aim and according procedure in this section for clarity: First we define the minimal model ingredients. Then we carry out the transformation of the Hamiltonian to bosonic coordinates up to bilinear terms (Sec. IV A 1) where, as compared to the Ising case, a doubling of the four-component boson fields occurs due to doublet degeneracy. The magnetic exciton energy bands are then obtained for our most general form of the Hamiltonian (Sec. IV A 2). It shows the effects of the various exchange couplings in the Hamiltonian in a transparent form which will be of great value for extracting their physical value from future experiments on singlet ground-state honeycomb materials. The bosonic approach also allows to compute the eigenvectors or Bloch states corresponding to the four exciton bands. These are essential inputs to identify their topological character via the Berry curvature and Chern number as carried out in Sec. V.

The exciton dispersions for our most general model are quite involved. Therefore, in Sec. IV A 3 we derive approximate mode energies for the weakly dispersive case sufficiently away from the soft-mode regime. We show that in this case the band energies are described by weakly dispersive separate sublattice modes coupled by the nearest-neighbor exchange. It is also important to consider the general solution for exciton bands for simpler cases to isolate the effect of sublattice symmetry breakings and the presence or absence of the various exchange terms, in particular the DM interaction. This will be carried out in Sec. IV B. At the special zone boundary points \mathbf{K}_{\pm} the exciton modes are degenerate unless the DM interaction is nonvanishing. The opening of a bulk gap due to the latter is an important issue in the honeycomb model because it provides the energy window for the appearance of topological edge modes. Therefore, we discuss the asymptotic form of bulk bands in the vicinity of the \mathbf{K}_{\pm} points to considerable detail in Sec. IV C.

A. Bosonic approach to the magnetic exciton bands of the singlet-doublet model

In contrast to the Ising model we focus here on the Bogoliubov approach to diagonalize the model Hamiltonian. The response function formalism can be applied accordingly and is described in Appendix C. Our aim is to show that due to the degeneracy of the excited state it allows for the existence of nontrivial topological character of magnetic exciton bands and associated appearance of edge modes within the gap of 2D bulk modes.

1. Model Hamiltonian and transformation to bosonic coordinates

The singlet-doublet model for honeycomb magnetic excitons leads to additional possibilities because of its xy -type exchange structure as enforced by the selection rules of Eq. (2). They show that in this model two of the total angular momentum operators J_x, J_y have nonzero matrix elements complementary to the previous singlet-singlet case that involves only J_z . Because the centers of second-neighbor bonds are not inversion centers in any case this opens the possibility for asymmetric DM exchange $H_{DM} = \sum_{\langle\langle ij \rangle\rangle} v_{ij} D_J (J_{ix} J_{jy} - J_{iy} J_{jx})$ according to Moriya rules [54]. Here we defined $D_J = (g_J - 1)^2 D$ ($g_J =$ Landé factor) as the original DM spin-exchange constant D projected to the lowest angular momentum multiplet ($J = 4$) considered in this work. It has to be staggered along each bond direction as expressed by $v_{ij} = \pm 1$, i.e., second neighbors $(-\tilde{\delta}_i, \tilde{\delta}_i)$ ($i = 1 - 3$) have DM exchange $(-D_J^A, D_J^A)$ on A sublattice and conversely $(D_J^B, -D_J^B)$ on the B sublattice. (Fig. 1). The total Hamiltonian in the Γ_2 - Γ_3 model is then given by

$$H = \sum_{\Gamma\sigma i} E_{\Gamma}^{\sigma} |\Gamma_{\sigma i}\rangle \langle \Gamma_{\sigma i}| - \sum_{\langle ij \rangle} I_{\sigma} (J_{iA}^x J_{jB}^x + J_{iA}^y J_{jB}^y) - \sum_{\langle\langle ij \rangle\rangle\sigma} I_2^{\sigma} (J_{i\sigma}^x J_{j\sigma}^x + J_{i\sigma}^y J_{j\sigma}^y) + \sum_{\langle\langle ij \rangle\rangle\sigma} v_{ij} D_J^{\sigma} (J_{i\sigma}^x J_{j\sigma}^y - J_{i\sigma}^y J_{j\sigma}^x). \quad (21)$$

Here we formulated the most general case of the model with first- ($\langle ij \rangle$) and second- ($\langle\langle ij \rangle\rangle$) neighbor exchange. We have in mind symmetric and asymmetric (DM) exchange interactions that are mediated by conduction electrons [48,55]. Further allowed exchange interactions like Kitaev terms or

symmetric terms off diagonal in momentum components are suppressed here to keep the number of model constants at a minimum and to isolate the effect of the DMI term. The CEF splittings as well as the three types of interactions are assumed to be sublattice dependent. As in the Ising case this may be caused by a different chemical environment of the two sublattice sites when the bare 2D honeycomb lattice of $4f$ ions is integrated into a larger 3D structure. We treat this model again by using the bosonic representation which is now defined by ($J_{\pm} = J_x \pm iJ_y$)

$$J_{+}^{iA} = \sqrt{2} \tilde{m}_A (a_{i+}^{\dagger} + a_{i-}), \quad J_{+}^{iB} = \sqrt{2} \tilde{m}_B (b_{i+}^{\dagger} + b_{i-}), \\ J_{-}^{iA} = \sqrt{2} \tilde{m}_A (a_{i-}^{\dagger} + a_{i+}), \quad J_{-}^{iB} = \sqrt{2} \tilde{m}_B (b_{i-}^{\dagger} + b_{i+}). \quad (22)$$

We notice that there is an additional degree of freedom $\lambda = \pm$ corresponding to the two doublet components $|\Gamma_3^{\lambda}\rangle$ represented by the $a_{i\lambda}^{\dagger}, b_{i\lambda}^{\dagger}$ creation operators. Only for some special cases this will remain a degeneracy index throughout the Brillouin zone (BZ) for the diagonalized excitonic eigenmodes.

Now again we introduce the Fourier-transformed bosonic operators $a_{\mathbf{k}\lambda}, b_{\mathbf{k}\lambda}$ and conjugates and express the Hamiltonian of Eq. (21) through them by using Eq. (22). We finally obtain

$$\hat{H} = \frac{1}{2} \sum_{\mathbf{k}\lambda} \phi_{\mathbf{k}\lambda}^{\dagger} \hat{h}_{\mathbf{k}\lambda} \phi_{\mathbf{k}\lambda} + E_0, \quad (23)$$

with $\phi_{\mathbf{k}\lambda} = (a_{\mathbf{k}\lambda}, b_{\mathbf{k}\lambda}, a_{-\mathbf{k}\bar{\lambda}}^{\dagger}, b_{-\mathbf{k}\bar{\lambda}}^{\dagger})^T$. Here we defined $\bar{\lambda} = -\lambda$ and $E_0 = N(\Delta_A + \Delta_B)$. Similar to the Ising-type model the four spinor components satisfy bosonic commutation relations $[\phi_n(\mathbf{k}\lambda), \phi_m^{\dagger}(\mathbf{k}'\lambda')] = \sum_z^{mm} \delta_{\mathbf{k}\mathbf{k}'} \delta_{\lambda\lambda'}$ where the 4×4 diagonal matrix is defined above in Eq. (19). In this representation we now have

$$\hat{h}_{\mathbf{k}\lambda} = \begin{pmatrix} \Delta_A - \bar{I}_D^A(\mathbf{k}\lambda) & -\bar{I}_N^*(\mathbf{k}) & -\bar{I}_D^A(\mathbf{k}\lambda) & -\bar{I}_N^*(\mathbf{k}) \\ -\bar{I}_N(\mathbf{k}) & \Delta_B - \bar{I}_D^B(\mathbf{k}\lambda) & -\bar{I}_N(\mathbf{k}) & -\bar{I}_D^B(\mathbf{k}\lambda) \\ -\bar{I}_D^A(-\mathbf{k}\bar{\lambda}) & -\bar{I}_N(-\mathbf{k}) & \Delta_A - \bar{I}_D^A(-\mathbf{k}\bar{\lambda}) & -\bar{I}_N(-\mathbf{k}) \\ -\bar{I}_N^*(-\mathbf{k}) & -\bar{I}_D^B(-\mathbf{k}\bar{\lambda}) & -\bar{I}_N^*(-\mathbf{k}) & \Delta_B - \bar{I}_D^B(-\mathbf{k}\bar{\lambda}) \end{pmatrix}. \quad (24)$$

Here the intrasublattice (D) and intersublattice (N) sublattice interactions are defined by

$$\bar{I}_D^A(\mathbf{k}\lambda) = \tilde{m}_A^2 I_D^A(\mathbf{k}\lambda), \\ I_D^A(\mathbf{k}\lambda) = (z_2 I_2^A) \gamma_2(\mathbf{k}) + \lambda (z_2 D_J^A) \tilde{\gamma}_D(\mathbf{k}) \\ = I_D^A(-\mathbf{k}\bar{\lambda}) = I_D^B(-\mathbf{k}\lambda), \\ \bar{I}_D^B(\mathbf{k}\lambda) = \tilde{m}_B^2 I_D^B(\mathbf{k}\lambda), \\ I_D^B(\mathbf{k}\lambda) = (z_2 I_2^B) \gamma_2(\mathbf{k}) - \lambda (z_2 D_J^B) \tilde{\gamma}_D(\mathbf{k}) \\ = I_D^B(-\mathbf{k}\bar{\lambda}) = I_D^A(-\mathbf{k}\lambda), \\ \bar{I}_N(\mathbf{k}) = \tilde{m}_A \tilde{m}_B I_N(\mathbf{k}), \quad I_N(\mathbf{k}) = (zI) \gamma(\mathbf{k}). \quad (25)$$

2. General case for magnetic exciton dispersion

Again for numerical computation it is convenient to use (now generally five) model parameters $v_s =$

$(\tilde{m}_A \tilde{m}_B I), v_s^{\sigma} = (\tilde{m}_s^2 I_s^{\sigma})$, and $v_D^{\sigma} = (\tilde{m}_s^2 I_D^{\sigma})$ and likewise $|\bar{I}_N(\mathbf{k})| = (z v_s) \gamma(\mathbf{k}), \bar{I}_D^A(\mathbf{k}\lambda) = (z_2 v_2^A) \gamma_2(\mathbf{k}) + \lambda (z_2 v_D^A) \tilde{\gamma}_D(\mathbf{k})$, and $\bar{I}_D^B(\mathbf{k}\lambda) = (z_2 v_2^B) \gamma_2(\mathbf{k}) - \lambda (z_2 v_D^B) \tilde{\gamma}_D(\mathbf{k})$ (see also Appendix B). Note the sign of the DM term changes with sublattice inversion and Γ_3 degeneracy index which leads to the symmetry $\bar{\lambda} \tilde{\gamma}_D(-\mathbf{k}) = \lambda \tilde{\gamma}_D(\mathbf{k})$ which has been used in the construction of the Hamiltonian matrix (24). The excitonic eigenmodes in the present general model are then, similar as in previous section, obtained by solving $|\Sigma_z \hat{h}_{\mathbf{k}} - \omega| = 0$. The solution leads to a closed form of their dispersions $\omega_{\kappa}^2(\mathbf{k}\lambda)$ ($\kappa = \pm$), given by a formally similar expression as Eq. (9) in the zero-temperature limit:

$$\omega_{\pm}^2(\mathbf{k}\lambda) = \frac{1}{2} [\omega_A^2(\mathbf{k}\lambda) + \omega_B^2(\mathbf{k}\lambda)] \pm \left[\frac{1}{4} [\omega_A^2(\mathbf{k}\lambda) - \omega_B^2(\mathbf{k}\lambda)]^2 + 4 \tilde{m}_A^2 \tilde{m}_B^2 \Delta_A \Delta_B |I_N(\mathbf{k})|^2 \right]^{\frac{1}{2}} \quad (26)$$

with

$$\omega_\sigma^2(\mathbf{k}\lambda) = \Delta_\sigma [\Delta_\sigma - 2\tilde{m}_\sigma^2 I_D^\sigma(\mathbf{k}\lambda)].$$

It is, however, distinct from the singlet-singlet model in the following aspects. First, in contrast to the latter the singlet-doublet model can realize the presence of a DM interaction in the intrasublattice part because two components J_x, J_y have nonzero matrix elements \tilde{m} between Γ_2 and Γ_3 . Second, due to the excited state Γ_3 being a doublet ($\lambda = \pm$) the number of modes doubles to four. They are still degenerate at each \mathbf{k} point for zero DM interaction. For nonzero D_j^σ the modes still fulfill the symmetry relation $\omega_\pm^2(\mathbf{k}\lambda) = \omega_\pm^2(-\mathbf{k}\bar{\lambda})$. Furthermore, the matrix elements \tilde{m}_σ are different from those of the singlet-singlet model (m_σ) [see below Eq. (2)]. Similar as in Sec. III A the above exciton dispersion $\omega_\kappa^2(\mathbf{k}\lambda)$ ($\kappa = \pm$) can be written more explicitly as

$$\begin{aligned} \omega_\pm^2(\mathbf{k}\lambda) = & \frac{1}{2}(\Delta_A^2 + \Delta_B^2) - [\tilde{m}_A^2 \Delta_A I_D^A(\mathbf{k}\lambda) + \tilde{m}_B^2 \Delta_B I_D^B(\mathbf{k}\lambda)] \\ & \pm \left\{ \left[\frac{1}{2}(\Delta_A^2 - \Delta_B^2) - [\tilde{m}_A^2 \Delta_A I_D^A(\mathbf{k}\lambda) \right. \right. \\ & \left. \left. - \tilde{m}_B^2 \Delta_B I_D^B(\mathbf{k}\lambda)] \right]^2 + 4\tilde{m}_A^2 \tilde{m}_B^2 \Delta_A \Delta_B |I_N(\mathbf{k})|^2 \right\}^{\frac{1}{2}}. \end{aligned} \quad (27)$$

When the DM interaction is set to zero and we replace $\tilde{m}_\sigma \rightarrow m_\sigma$ and the degeneracy in the Γ_3^\pm index λ is ignored, this becomes equivalent to the general case of the Ising-type singlet-singlet model [Eq. (9)]. The temperature dependence of the dispersions can be incorporated by reminding (Sec. III B) that it enters in a parametric way by introducing effective matrix elements $\tilde{m}_\sigma^2 \rightarrow \tilde{m}_\sigma^2 \tanh \frac{\Delta_\sigma}{2T} (1 + f_\sigma)^{-1}$ where the correction factor with $f_\sigma = \frac{1}{2}(1 - \tanh \frac{\Delta_\sigma}{2T})$ is due to the twofold degeneracy of the Γ_3 doublet. This may be concluded from the complementary RPA approach for the xy -type model (Appendix C).

3. Approximate dispersions from a reduced Hamiltonian

The exact expressions for the exciton dispersions of the 4×4 Hamiltonian in Eq. (24) as given by Eq. (26) exhibit the redundancy or doubling which is typical for the Bogoliubov technique, i.e., they appear in pairs ($+\omega_\kappa, -\omega_\kappa$) (in the RPA response function technique they correspond to poles at positive and negative frequencies). These expressions may be considerably simplified if certain conditions are fulfilled: (i) the dispersion width is small compared to the CEF excitation energy Δ which means that throughout the BZ it is far from soft-mode behavior. This requires $\tilde{m}_\sigma^2 I_D^\sigma(\mathbf{k}\lambda)/\Delta_\sigma \ll 1$. In this case ($+\omega_\kappa, -\omega_\kappa$) pairs are sufficiently apart which means they correspond approximately to the solution of the diagonal 2×2 blocks in $\Sigma_z \hat{h}_{\mathbf{k}\lambda}$. This approximation is reasonable if $\Delta_{A,B}$ CEF splittings are not too different. More precisely, if we define the various averages $\Delta_{\text{av}} = \frac{1}{2}(\Delta_A + \Delta_B)$, $\bar{\Delta} = (\Delta_A \Delta_B)^{\frac{1}{2}}$, $\Delta_m = [\frac{1}{2}(\Delta_A^2 + \Delta_B^2)]^{\frac{1}{2}}$ the conditions $\bar{\Delta}/\Delta_{\text{av}} \simeq 1$, $\Delta_{\text{av}}/\Delta_m \simeq 1$ should be respected. For $\Delta_A = \Delta_B$ they hold identically. With these premises the exact dispersions of Eq. (27) may be approximated by the (positive)

exciton energies

$$\begin{aligned} \omega_\pm^r(\mathbf{k}\lambda) = & \frac{1}{2}[\omega_{A0}(\mathbf{k}\lambda) + \omega_{B0}(\mathbf{k}\lambda)] \\ & \pm \frac{1}{2} \left[[\omega_{A0}(\mathbf{k}\lambda) - \omega_{B0}(\mathbf{k}\lambda)]^2 + 4\tilde{m}_A^2 \tilde{m}_B^2 |I_N(\mathbf{k})|^2 \right]^{\frac{1}{2}}, \\ \omega_{\sigma 0}(\mathbf{k}\lambda) = & \Delta_\sigma - \tilde{m}_\sigma^2 I_D^\sigma(\mathbf{k}\lambda). \end{aligned} \quad (28)$$

It can be seen easily that these modes correspond directly to the eigenvalues of the reduced 2×2 Hamiltonian

$$\hat{h}_{\mathbf{k}\lambda}^r = \begin{pmatrix} \Delta_A - \bar{I}_D^A(\mathbf{k}\lambda) & -\bar{I}_N^*(\mathbf{k}) \\ -\bar{I}_N(\mathbf{k}) & \Delta_B - \bar{I}_D^B(\mathbf{k}\lambda) \end{pmatrix}, \quad (29)$$

which corresponds only to the diagonal blocks in the 4×4 Hamiltonian (24). Effectively, the nondiagonal blocks in $\Sigma_z \hat{h}_{\mathbf{k}\lambda}$ have the effect of coupling the positive and negative frequency solutions $\pm\omega_\kappa^r(\mathbf{k}\lambda)$ ($\kappa = \pm$) of the two diagonal blocks and produce the exact solutions $\pm\omega_\kappa(\mathbf{k}\lambda)$ of Eq. (26) or (27). The approximate treatment of this section provides a convenient starting point for calculating the topological boundary modes in continuum approximation as carried out in Sec. V B.

B. Special cases of the singlet-doublet model

Now we return to the exact and general dispersion model equations (26) and (27). We will discuss a few interesting special cases which have either less coupling terms and/or more sublattice equivalences of model parameters.

1. First special case

Here we assume the absence of symmetric second-neighbor exchange and sublattice equivalence of DM terms: $I_\sigma^s = 0$, $I_D^s = I_D$.

In this case Eq. (27) reduces to the simpler form

$$\begin{aligned} \omega_\pm^2(\mathbf{k}\lambda) = & \frac{1}{2}(\Delta_A^2 + \Delta_B^2) - \lambda(z_2 v_D)(\Delta_A - \Delta_B) \tilde{\gamma}_D(\mathbf{k}) \\ & \pm \left\{ \frac{1}{4}(\Delta_A + \Delta_B)^2 [(\Delta_A - \Delta_B) - 2\lambda(z_2 v_D) \tilde{\gamma}_D(\mathbf{k})]^2 \right. \\ & \left. + 4\Delta_A \Delta_B (z v_s)^2 |\gamma(\mathbf{k})|^2 \right\}^{\frac{1}{2}}, \end{aligned} \quad (30)$$

where we introduced abbreviations $v_s = \tilde{m}^2 I$ and $v_D = \tilde{m}^2 D_J$. This form gives convenient access to the mode dispersions around the inequivalent zone boundary points \mathbf{K}_\pm . The essential part is the ‘‘mass term’’ (first term in curly brackets) given by

$$M(\mathbf{K}_\pm, \lambda) = \frac{1}{2}(\Delta_A + \Delta_B)[(\Delta_A - \Delta_B) - 2\lambda(z_2 v_D) \tilde{\gamma}_D(\mathbf{K}_\pm)], \quad (31)$$

which may be both positive or negative depending on conditions and valley position \mathbf{K}_\pm (Secs. IV B and V). The above equation shows that in general the λ degeneracy resulting from Γ_3^\pm doublet is lifted if, first, the CEF splittings are inequivalent and, second, the DM term is nonzero. This becomes also clear from the next special case.

2. Second special case

Here, in addition to the first case we assume the equivalence $\Delta_A = \Delta_B = \Delta$: Then we obtain the further simplified dispersion form

$$\omega_{\pm}^2(\mathbf{k}) = \Delta \left\{ \Delta \pm 2[(z_2 v_D)^2 \tilde{\gamma}_D(\mathbf{k})^2 + (z v_s)^2 |\gamma(\mathbf{k})|^2]^{\frac{1}{2}} \right\}. \quad (32)$$

Due to the equivalent CEF splittings the dispersions now retain the twofold degeneracy ($\lambda = \pm$) throughout the BZ, therefore, this index has been suppressed. As a result, only two dispersion curves ($\kappa = \pm$ due to two sublattices) are present. We also give the simplified dispersion of the reduced model from Eq. (28) for the same special case:

$$\omega_{\pm}^r(\mathbf{k}) = \Delta \pm [(z_2 v_D)^2 \tilde{\gamma}_D(\mathbf{k})^2 + (z v_s)^2 |\gamma(\mathbf{k})|^2]^{\frac{1}{2}}. \quad (33)$$

It is obviously the approximation to Eq. (32) for moderate dispersion ($v_s, v_D \ll \Delta$) far from the soft-mode regime.

C. Expansions of magnetic exciton dispersion around \mathbf{K}_{\pm} valleys

It is important to understand the behavior of exciton bands around the inequivalent valley points \mathbf{K}_{\pm} because they influence their topological character. It is largely determined by the expansion of structure functions in Appendix E.

1. General case

For the most general case of parameter sets in Eq. (27) we obtain the following result (now $\kappa = \pm$ and $\lambda = \pm$ for the two mode pairs and \mathbf{K}_{\pm} referring now to the two boundary points):

$$\omega_D^{\kappa}(\mathbf{K}_{\pm}, \lambda, \hat{q}) = \omega_{D0}^{\kappa}(\mathbf{K}_{\pm}, \lambda) + \kappa \{ M(\mathbf{K}_{\pm}, \lambda)^2 + 3\pi^2 \Delta_A \Delta_B (v_s \hat{q})^2 \}^{\frac{1}{2}}, \quad (34)$$

where we use the scaled momentum $\hat{q} = (q_x^2 + q_y^2)^{\frac{1}{2}} / (\pi/a)$ with respect to the \mathbf{K}_{\pm} Dirac points, i.e., $\mathbf{k} = \mathbf{K}_{\pm} + \mathbf{q}$. The generally distinct energies of the latter are given by ($v_{\sigma} = \tilde{m}_{\sigma}^2 I_{\sigma}^2$, $v_D^{\sigma} = \tilde{m}_{\sigma}^2 D_{\sigma}^{\sigma}$ and $\sigma = A, B$)

$$\omega_{D0}^{\kappa}(\mathbf{K}_{\pm}, \lambda) = \frac{1}{2}(\Delta_A^2 + \Delta_B^2) + 3(\Delta_A v_A + \Delta_B v_B) \pm \lambda \sqrt{3}(\Delta_A v_D^A - \Delta_B v_D^B), \quad (35)$$

and depend on valley (\pm) and Γ_3 degeneracy index λ . The splitting of bands at \mathbf{K}_{\pm} is determined by the mass term of the square root in Eq. (34) given by

$$M(\mathbf{K}_{\pm}, \lambda) = \frac{1}{2}(\Delta_A^2 - \Delta_B^2) + 3(\Delta_A v_A - \Delta_B v_B) \pm \lambda \sqrt{3}(\Delta_A v_D^A + \Delta_B v_D^B). \quad (36)$$

The last term leads to different mass values and (generally) splittings at \mathbf{K}_{\pm} due to its different signs. The size of the mode splitting $\delta(\mathbf{K}_{\pm})$ at zone boundary points is given by the difference of the mass terms for $\lambda = \pm$, i.e., $\delta(\mathbf{K}_{\pm}) = \pm 2\sqrt{3}(\Delta_A v_D^A + \Delta_B v_D^B)$. It is only finite when the DM interaction is nonzero and changes sign between \mathbf{K}_{\pm} . For the equivalent A, B sublattice model then $\delta(\mathbf{K}_{\pm}) = \pm 4\sqrt{3}\Delta v_D$ the splitting provides a direct means to determine the size of the DMI. This originates in the different signs of the DM structure function $\tilde{\gamma}_D(\mathbf{K}_{\pm}) = \mp \frac{3\sqrt{2}}{2}$ (Appendix E). If the mass term vanishes, the exciton bands are all degenerate at \mathbf{K}_{\pm}

and show a linear dispersion around it due to the last term in Eq. (34).

Obviously interchanging valley \mathbf{K}_{\pm} position and simultaneously the Γ_3 states $\lambda = \pm$ leaves the Dirac point energy and mass term invariant, i.e., they fulfill the symmetry $\omega_{D0}(\mathbf{K}_{\pm}, \lambda) = \omega_{D0}(\mathbf{K}_{\mp}, -\lambda)$ and $M(\mathbf{K}_{\pm}, \lambda) = M(\mathbf{K}_{\mp}, -\lambda)$.

As in the previous subsection it is again useful to consider the two special cases with reduced parameter set.

2. First special case

Here only the CEF splittings are different on A and B . Then we can simplify, defining the average gap by $\Delta_{av} = \frac{1}{2}(\Delta_A + \Delta_B)$, we have

$$\omega_{D0}^{\kappa}(\mathbf{K}_{\pm}, \lambda) = \frac{1}{2}(\Delta_A^2 + \Delta_B^2) \pm \lambda \sqrt{3} v_D (\Delta_A - \Delta_B), \quad (37)$$

$$M(\mathbf{K}_{\pm}, \lambda) = \Delta_{av} [(\Delta_A - \Delta_B) \pm \lambda 2\sqrt{3} v_D].$$

The square of the exciton dispersion is then given by

$$\omega_D^{\kappa}(\mathbf{K}_{\pm}, \lambda, \hat{q}) = \omega_{D0}^{\kappa}(\mathbf{K}_{\pm}, \lambda) + \kappa [M(\mathbf{K}_{\pm}, \lambda)^2 + D_0^2 \hat{q}^2]^{\frac{1}{2}}, \quad (38)$$

$$D_0 = \sqrt{3}\pi (\Delta_A \Delta_B)^{\frac{1}{2}} v_s.$$

It is instructive to evaluate directly the dispersion $\omega_D^{\kappa}(\mathbf{K}_{\pm}, \lambda, \hat{q})$ at small \hat{q} for the case of finite mass term

$$\omega_D^{\kappa}(\mathbf{K}_{\pm}, \lambda, \hat{q}) = \omega_{D0}^{\kappa}(\mathbf{K}_{\pm}, \lambda) + \kappa \frac{D_0^2}{4|M|\omega_{D0}} \hat{q}^2, \quad (39)$$

$$\omega_{D0}^{\kappa}(\mathbf{K}_{\pm}, \lambda) = \omega_{D0}(\mathbf{K}_{\pm}, \lambda) + \kappa \frac{|M|}{2\omega_{D0}}.$$

The first term describes the split energies at the Dirac points or valleys \mathbf{K}_{\pm} [first of Eq. (37)]. For $\Delta_A \neq \Delta_B$ in Eq. (37) there are four distinct energies at each \mathbf{K}_{\pm} indexed by (κ, λ) and four corresponding split parabolic exciton bands around them [Figs. 4(b)–4(d)].

3. Second special case

As in the previous Sec. IV B 2 we assume now in addition equal CEF splittings Δ on both A and B sublattices these expressions further simplify in an obvious manner with $\omega_{D0} = \Delta$, $M(\mathbf{K}_{\pm}, \lambda) = \pm \lambda 2\sqrt{3}\Delta v_D$ and $D_0 = \sqrt{3}\pi \Delta v_s$ which results in two degenerate ($\lambda = \pm$) pairs of modes. If we turn off the DM interaction ($v_D = 0$) the mass term vanishes and we have to go back to Eq. (38), which then leads to

$$\omega_D^{\kappa}(\hat{q}) = \Delta + \kappa \frac{\sqrt{3}}{2} \pi v_s |\hat{q}|, \quad (40)$$

which describes two Dirac half-cone ($\kappa = \pm$) exciton dispersions centered around the CEF excitation energy Δ which are identical for \mathbf{K}_{\pm} and retain the twofold degeneracy with respect to Γ_3 index λ .

V. TOPOLOGICAL PROPERTIES OF MAGNETIC EXCITON MODES

Like any kind dispersive modes, in particular magnons in the ferromagnetic honeycomb lattice, the paramagnetic exciton bands studied here can be characterized according to their topological properties. For 2D systems the relevant quantities

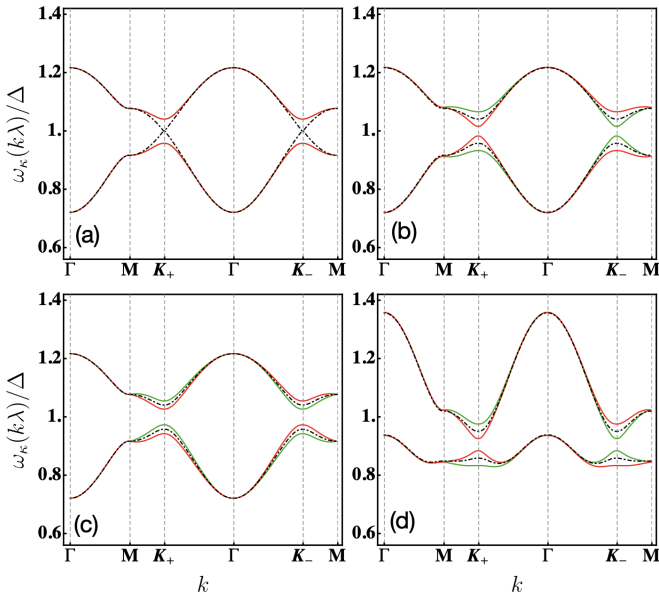


FIG. 4. Exciton dispersions $\omega_\kappa^\lambda(\mathbf{k})$ ($T = 0.1$) and their typical behavior of gap formation at \mathbf{K}_\pm for xy -type model for $\Gamma MK_+ \Gamma K_- M$ path in the BZ. Common parameters are $\Delta = 1$, $v_s = 0.08$. (a) $v_2 = 0$, $\epsilon = 0$, dashed line: $v_d = 0$; full line: $v_d = 0.008$. The DM interaction opens gaps at \mathbf{K}_\pm but keeps the twofold $\Gamma_3^\pm(\lambda)$ degeneracy throughout the BZ if parameters are identical on sublattices A and B . (b) Dashed line: $v_d = 0.008$, $\epsilon = 0$; full line: $v_d = 0.008$, $\epsilon = 0.025$ with $\Delta_{A,B} = \Delta(1 \pm \epsilon)$. For inequivalent $\Delta_{A,B}$ the λ degeneracy is generally lifted (green: $\lambda = +$; red: $\lambda = -$) but prevails along the ΓM direction. This is due to the band crossing along $K_+ K_-$ segment at $k_y = 0$. As a consequence, the band ordering (green/red) is inverted at \mathbf{K}_+ and \mathbf{K}_- . (c) Here $\Delta_A = \Delta_B$ but $v_d^{A,B} = v_d(1 \pm \epsilon_d)$ is different with $\epsilon_d = 0.35$. This also lifts the \mathbf{K}_\pm degeneracies but with different sequence of bands. (d) This panel corresponds to (b) but now finite (AF) $v_2 = -0.03$ included which destroys the approximate reflection symmetry around $\omega = \Delta$.

to investigate for this purpose are the Berry curvature and the associated Chern number topological invariant.

A. Berry curvature and Chern numbers

The topological character of magnetic exciton bands is determined by Berry curvature obtained from the effective

$$\Omega_n^z(\mathbf{k}) = \sum_{m \neq n} \frac{i[\langle n\mathbf{k} | \hat{h}_\mathbf{k}^x | m\mathbf{k} \rangle \Sigma_z^{mm} \langle m\mathbf{k} | \hat{h}_\mathbf{k}^y | n\mathbf{k} \rangle - \langle n\mathbf{k} | \hat{h}_\mathbf{k}^y | m\mathbf{k} \rangle \Sigma_z^{mm} \langle m\mathbf{k} | \hat{h}_\mathbf{k}^x | n\mathbf{k} \rangle]}{[\omega_n(\mathbf{k}) - \omega_m(\mathbf{k})]^2}. \quad (44)$$

The Chern number characterizing the topological character of magnetic exciton bands (reintroducing now the Γ_3 index λ) is then obtained by $[n = (\kappa, \tau)]$

$$C_n(\lambda) = \frac{1}{2\pi} \int_{\text{BZ}} d\mathbf{k} \Omega_n^z(\mathbf{k}, \lambda). \quad (45)$$

The \mathbf{k} dependence of $\hat{h}_\mathbf{k}$ in Eqs. (19) and (24) stems entirely from that of the structure functions. Therefore, the gradients $\hat{h}_{\mathbf{k}\lambda}^\alpha = \partial \hat{h}_\mathbf{k} / \partial k_\alpha$ ($\alpha = x, y$) required in Eq. (44) may be computed analytically (Appendix F). Because the

Hamiltonian matrix $\tilde{h}(\mathbf{k}\lambda) = \Sigma_z \hat{h}(\mathbf{k}\lambda)$ [Eq. (24)] which has, for each $\lambda = \pm$ two positive $\omega_\kappa(\mathbf{k}, \lambda)$ ($\kappa = \pm, \tau = +$) and two negative $-\omega_\kappa(\mathbf{k}, \lambda)$ ($\kappa = \pm, \tau = -$) eigenvalues [from Eq. (27)]. The latter are a result of the doubling of degrees of freedom in the Bogoliubov method [56]. The index $\tau = \pm$ corresponds to the positive or negative set [the sign in front of $\tau\omega_\kappa(\mathbf{k}, \lambda)$]. Then we may combine positive and negative solutions to a single index $n = (\kappa, \tau) = 1-4$ resulting from sublattice degree of freedom and Bogoliubov doubling. This is done for each $\lambda = \pm$ subspace resulting from the Γ_3 CEF degrees of freedom. The index λ is suppressed as a dummy index in the following that simply refers to two different sets of bands (which may be completely degenerate in the BZ as discussed before in special cases). Physical relevant excitations are only the positive energy solutions. The negative solutions, however, do appear in the calculation of the topological quantities.

The topological properties of these bands are described by the Berry curvature given by

$$\Omega_n(\mathbf{k}) = \nabla_\mathbf{k} \times i \langle n(\mathbf{k}) | \nabla_\mathbf{k} | n(\mathbf{k}) \rangle, \quad (41)$$

where $|n(\mathbf{k})\rangle$ denote the eigenvectors or Bloch functions corresponding to the eigenvalue equation $\tilde{h}(\mathbf{k})|n(\mathbf{k})\rangle = \omega_n(\mathbf{k})|n(\mathbf{k})\rangle$. This may also be written as $[\omega_n(\mathbf{k}) > 0]$ [57]

$$\Omega_n(\mathbf{k}) = i \sum_{m \neq n} \langle m\mathbf{k} | \Sigma_z \nabla_\mathbf{k} | n\mathbf{k} \rangle^* \Sigma_z^{mm} \times \langle m\mathbf{k} | \Sigma_z \nabla_\mathbf{k} | n\mathbf{k} \rangle. \quad (42)$$

An alternative expression more useful for numerical computation is given by [57]

$$\Omega_n(\mathbf{k}) = \sum_{m \neq n} \frac{i \langle n\mathbf{k} | \nabla_\mathbf{k} \hat{h}_\mathbf{k} | m\mathbf{k} \rangle \Sigma_z^{mm} \times \langle m\mathbf{k} | \nabla_\mathbf{k} \hat{h}_\mathbf{k} | n\mathbf{k} \rangle}{[\omega_n(\mathbf{k}) - \omega_m(\mathbf{k})]^2}, \quad (43)$$

where the sum over m runs over eigenstates with positive and negative energies $\omega_m(\mathbf{k})$. Using the explicit expression of $\hat{h}_\mathbf{k}$ and its gradient $\nabla_\mathbf{k} \hat{h}_\mathbf{k}$ as well as the eigenvalues and eigenvectors of $\tilde{h}_\mathbf{k} = \Sigma_z \hat{h}_\mathbf{k}$ the Berry curvature $\Omega_n(\mathbf{k})$ may be computed numerically from the above expression. For the 2D honeycomb models only the $\Omega_n^z(\mathbf{k})$ component is nonzero. Explicitly, it is given by

eigenvectors in Eq. (44) have to be obtained numerically, this is also necessary for the Berry curvature. It is shown in Fig. 6 for some typical parameters for the positive bands in the irreducible BZ and will be discussed in more detail in Sec. VI. There are two typical cases to be observed with Berry curvature maximum (or negative minimum) located at the \mathbf{K}_\pm zone boundary symmetry points, or at three (C_{3v} equivalent) of-symmetry points. Whether the Chern number (i.e., the integral of the Berry curvature over the irreducible BZ) is zero (topologically trivial) or nonzero

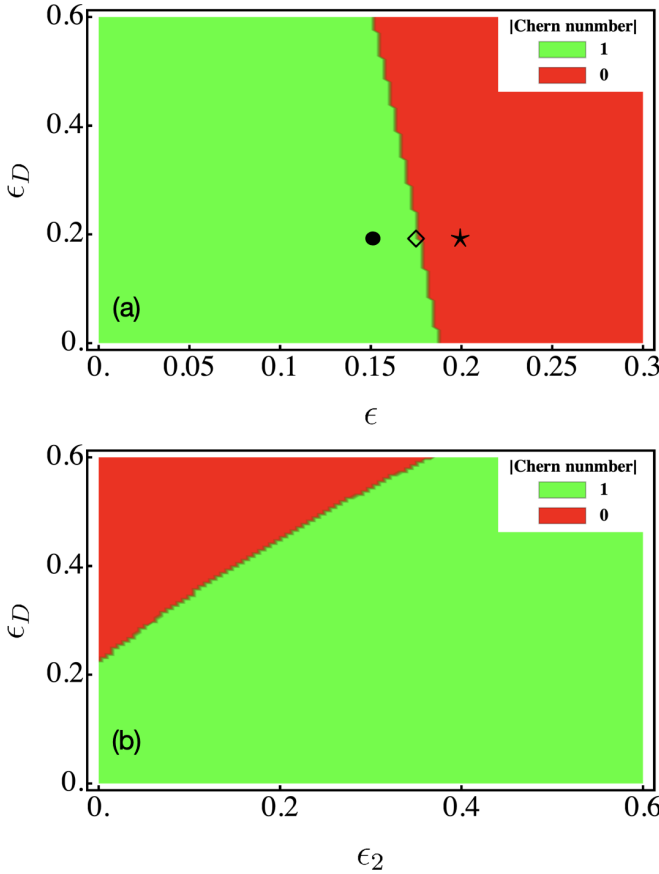


FIG. 5. Contour plot of Chern numbers as functions of (a) ϵ in $\Delta_{A,B} = \Delta(1 \pm \epsilon)$ and ϵ_D in $v_D^{A,B} = v_D(1 \pm \epsilon_D)$ by setting $\epsilon_2 = 0$ in $v_2^{A,B} = v_2(1 \pm \epsilon_2)$. Symbols \star , \diamond , \bullet correspond to values used in Figs. 6(a)–6(d), 6(e)–6(h), and 6(i)–6(l), respectively. (b) As functions of ϵ_D and ϵ_2 by setting $\epsilon = 0.175$. Common parameters are $\Delta = 1$, $v_s = 0.08$, $v_2 = -0.03$, and $v_D = 0.04$. The topological nontrivial bands are stable in the sublattice-equivalent cases, e.g., $(\epsilon, \epsilon_D) = (0, 0)$ and $(\epsilon_2, \epsilon_D) = (0, 0)$.

integer (topologically nontrivial) exciton bands depend to some extent on the amount of inversion symmetry breaking (difference of $\sigma = A, B$ sublattice parameters Δ_σ , v_2^σ , v_D^σ), as discussed in Sec. VI. For the sublattice-equivalent case when they are all equal the Chern numbers are all ± 1 for the four bands and therefore each of them is topologically nontrivial which should entail the existence of gapless 1D excitonic edge states inside the 2D bulk DM gap at \mathbf{K}_\pm . The symmetric case is conveniently accessible by a continuum approximation, i.e., small momentum approximation around \mathbf{K}_\pm . This will indeed predict the existence of edge states as we shall show now.

B. Topological edge modes in continuum approximation

An alternative and direct way to approach the nontrivial topology is provided by the explicit construction of excitonic magnetic edge states within the 2D bulk gap at \mathbf{K}_\pm valleys which decay exponentially into the bulk. We demonstrate this in the simplified approach mentioned before that neglects the interaction of $\pm\omega_n(\mathbf{k}\lambda)$ modes in the secular equation. This is acceptable as long one is not too close to a soft-

mode situation. It amounts to considering only the reduced 2×2 Hamiltonian of Eq. (29). For the reduced model we apply the continuum approximation around the \mathbf{K}_\pm by setting $\mathbf{k} = \mathbf{K}_\pm + \mathbf{q}'$ where \mathbf{q}' is expressed in the rotated Cartesian coordinate systems defined in Appendix E. We first focus on \mathbf{K}_+ . The q'_x direction corresponds to zigzag chain direction in real space which we consider as an edge of the semi-infinite honeycomb lattice. Then we have to replace the perpendicular coordinate according to $q'_y \rightarrow -i\partial_{y'}$ in the reduced Hamiltonian above. For the simplified equivalent sublattice case (ii) in Sec. IV B ($v_2 = 0$) we obtain

$$\hat{h}^r(q'_x\lambda, y) = \begin{pmatrix} \Delta + \lambda\delta_D & (zv_s)\xi(q'_x - \partial_{y'}) \\ (zv_s)\xi(q'_x + \partial_{y'}) & \Delta - \lambda\delta_D \end{pmatrix}, \quad (46)$$

where $\xi = \frac{a}{2\sqrt{3}}$ and $\lambda\delta_D = \lambda 3\sqrt{2}v_D$ describes the effect of the DM interaction which importantly has *opposite* sign on the two sublattices. As an ansatz wave function for the excitonic edge eigenstate we use $\mathbf{w}(q'_x, y) = \mathbf{w}_0 e^{iq'_x x'} e^{-\kappa_D y'}$. The corresponding eigenvalue equation $\hat{h}^r(q'_x\lambda, y)\mathbf{w}(q'_x, y) = \omega\mathbf{w}(q'_x, y)$ then leads to the secular equation

$$\begin{vmatrix} \Delta + \lambda\delta_D - \omega & (zv_s)\xi(q'_x + \kappa_D) \\ (zv_s)\xi(q'_x - \kappa_D) & \Delta - \lambda\delta_D - \omega \end{vmatrix} = 0, \quad (47)$$

which has λ degenerate solutions

$$\omega_\pm = \Delta \pm \left[[\delta_D^2 - (zv_s)^2 \xi^2 \kappa_D^2] + \xi^2 (zv_s)^2 q_x^2 \right]^{\frac{1}{2}}. \quad (48)$$

Choosing $\kappa_D = \frac{|\delta_D|}{zv_s \xi} = \frac{\sqrt{3}}{2} \frac{v_D}{v_s}$ we obtain gapless edge-mode dispersions ($\kappa = \pm$)

$$\omega_\kappa(q'_x) = \Delta + \kappa (zv_s)\xi |q'_x| = \Delta \pm \frac{\sqrt{3}}{2} \pi v_s |\hat{q}_x|, \quad (49)$$

where $\hat{q}_x = q'_x/(\pi/a)$. This describes a 1D Dirac cone of excitonic edge modes emerging from the Dirac point $\omega_{D0} = \Delta$ with momentum oriented along the zigzag chain direction. The calculation is equivalent for the \mathbf{K}_- value with the replacement $(\delta_D, \kappa_D) \rightarrow (-\delta_D, -\kappa_D)$ in Eq. (47) leading to the same dispersion for the edge modes around \mathbf{K}_- . The edge-mode dispersion approaches asymptotically the gapped bulk mode dispersion (for $\Delta_{A,B} = \Delta$) of Eq. (38) for $q'_y = 0$ and becomes identical to this mode [Eq. (40)] when the gap closes ($v_D \rightarrow 0$ and $\kappa_D \rightarrow 0$).

It is interesting to consider an alternative case of the simplified model without the second-neighbor DM exchange ($v_D = 0$) but instead including the second-neighbor symmetric exchange ($v_2 \neq 0$). In this case the essential difference from Eq. (47) is the lack of sign change in $\delta_2 = 3\sqrt{2}v_2$ between the sublattices leading simply to a renormalization of the CEF splitting $\tilde{\Delta} = \Delta + \delta_2$. Therefore, the secular equation has no solution for edge states for $q'_x \rightarrow 0$ and only bulk states are present. We conclude that the general structure of the magnetic exciton models discussed here always require a nonzero DM interaction for the existence of topological edge states.

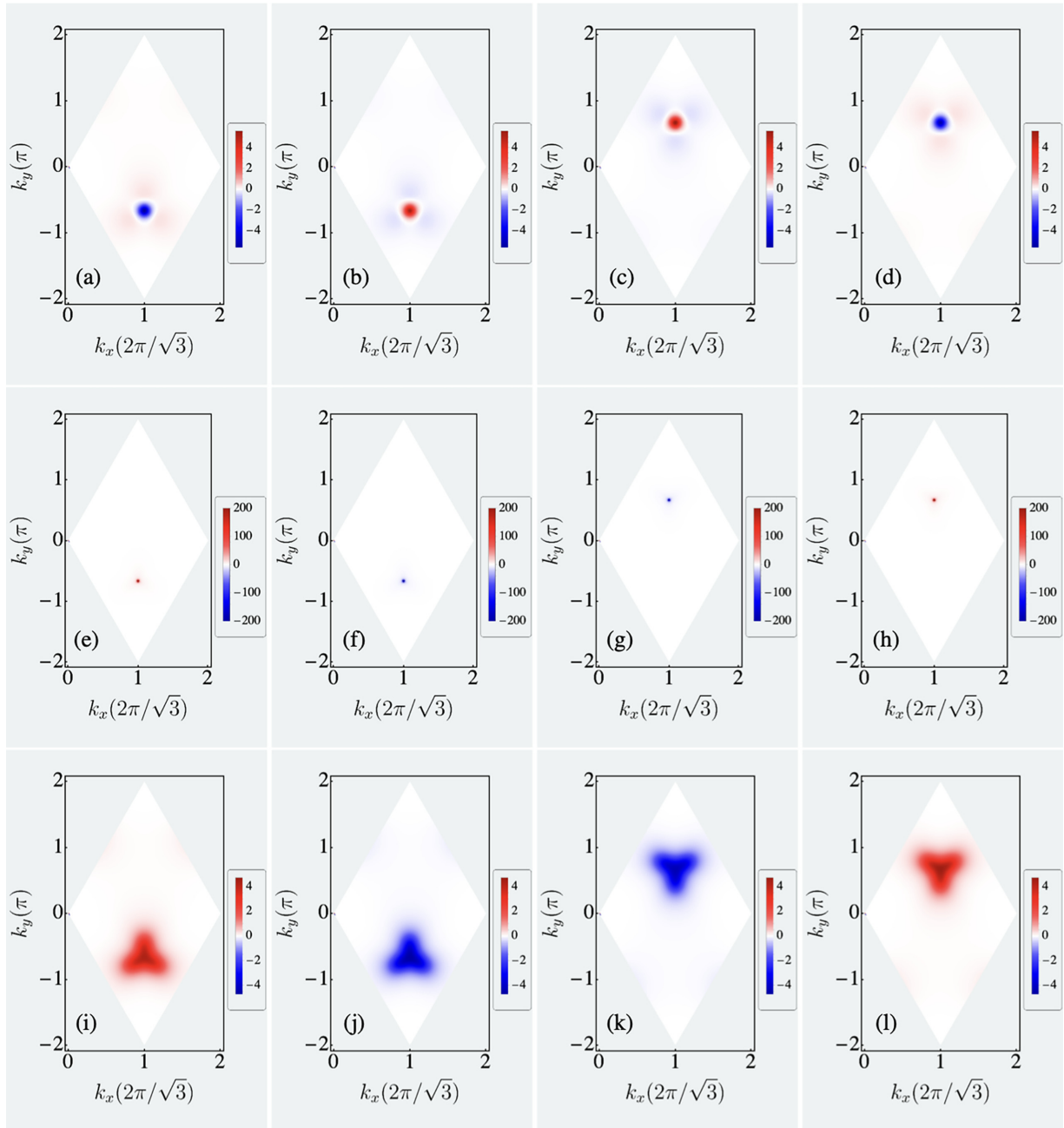


FIG. 6. Density plot of Berry curvature in BZ corresponding to bands $(\kappa, \lambda) = (+, +), (-, +), (+, -), (-, -)$ from left to right in each row according to decreasing energy for each λ . Parameters are same as in Fig. 5(a). First we show two cases according to symbols (\star, \diamond) in Fig. 5(a) to the right and left of the topological boundary. (a)–(d) Chern number 0 at the \star point $\epsilon = 0.2$ and $\epsilon_D = 0.2$ in Fig. 5(a); (e)–(h) Chern number ± 1 at the \diamond left boundary point $\epsilon = 0.175$ and $\epsilon_D = 0.2$ in Fig. 5(a). Berry curvature has both \pm sign in for each panel of (a)–(d) so the integration gives a zero Chern number, however, it shows only positive or negative values for each panel of (e)–(h) and therefore finite Chern number ± 1 . In (i)–(l) $\epsilon = 0.15$ is relatively small compared to ϵ_D leading to a shift of the Berry curvature extrema to three C_{3v} equivalent incommensurate positions closer to the M point, however, the Chern number still is ± 1 corresponding to \bullet in Fig. 5(a).

VI. DISCUSSION OF NUMERICAL RESULTS FOR THE xy -TYPE MODEL

We already discussed the magnetic excitons in the simple Ising-type model (Sec. III) and now focus on the more intricate results of the xy -type model (Sec. IV).

For a first inspection one may restrict to the special models of Sec. IV B. The restricted parameter set is then

given by CEF splitting energies Δ_A, Δ_B and the sublattice-equivalent interaction energy parameters $v_s = \tilde{m}^2 I$ and $v_D = \tilde{m}^2 D_J$ corresponding to first-neighbor ($z = 3$) (A - B) symmetric exchange and second-neighbor ($z_2 = 6$) (A - A, B - B) DM exchange. The energy unit for these parameters may be chosen as the average Δ and we use the representation $\Delta_{A,B} = \Delta(1 \pm \epsilon)$, etc. (Appendix B).

Some representative dispersion results for these special cases for the xy model are shown in Fig. 4. In Figs. 4(a) and 4(b) we also set intrasublattice $v_2 = 0$, therefore, the splitting of modes caused by intersublattice interaction v_s is nearly symmetric around Δ . In Fig. 4(a) when $\epsilon = 0$ the upper and lower modes ($\kappa = \pm$) inherit the twofold degeneracy with respect to the CEF Γ_3 index $\lambda = \pm$. If the DM interaction vanishes ($v_d = 0$) the two pairs of mode are fully degenerate at \mathbf{K}_\pm zone boundary points (dashed lines) but for nonvanishing v_d the degeneracy is lifted and a gap appears. The gap persists in the case of inequivalent CEF splittings ($\epsilon \neq 0$) [Fig. 4(b)]. Now the fourfold degeneracy is completely removed because $\lambda = \pm$ modes are no longer degenerate. This is also true when a finite v_2 is included which removes the approximate reflection symmetry of lower and upper branches [Fig. 4(d)]. Note the important point that in both cases the ordering of modes $\lambda = \pm$ (corresponding to the coloring green/red) is interchanged at \mathbf{K}_\pm . This is due to the symmetry $\omega_\kappa(\mathbf{k}, \lambda) = \omega(-\mathbf{k}, \bar{\lambda})$ and the fact that \mathbf{K}_- is equivalent to $-\mathbf{K}_+$. For comparison we also show a case where the CEF splittings are equivalent ($\epsilon = 0$) but the DM coupling strengths $v_D^{A,B}$ are not, again with $v_2 = 0$ [Fig. 4(c)]. It looks similar to Fig. 4(b) but the band ordering is changed such that the gaps at \mathbf{K}_\pm do not depend on λ in contrast to Fig. 4(b).

Now we discuss the topological properties of the magnetic exciton bands. The crucial role there is played by the DM interaction which opens the necessary gap at \mathbf{K}_\pm for nontrivial topology (nonzero Chern number). In the inversion-symmetric case with all A and B sublattice parameters equivalent the Chern number is always nonzero in the (v_s, v_D) plane as shown in Fig. 5. This agrees with the fact that in the inversion-symmetric case the continuum approximation shows the existence of zone boundary modes as shown in the previous section. The introduction of A and B sublattice asymmetry, e.g., by assuming different CEF splittings $\Delta_{A,B} = \Delta(1 \pm \epsilon)$ can destroy the topological state leading to vanishing Chern number as is shown in the example denoted by \star in Fig. 5 which shows that the inequivalence of $\Delta_{A,B}$ should stay below a threshold to achieve topologically nontrivial bands with $C = \pm 1$.

To obtain an intuition how the vanishing and nonzero Chern numbers are obtained we also plot the Berry curvature $\Omega_n^z(\mathbf{k}, \lambda)$ in the irreducible wedge of the BZ for the different sets of (positive energy) bands $\omega_n(\mathbf{k}, \lambda)$ with $n = (\kappa, \tau = +)$ leading to four panels in each row corresponding to all four choices of ($\lambda = \pm, \kappa = \pm$). We show these four panels for three cases corresponding to the trivial (a)–(d) [$C_n(\lambda) = 0$] and nontrivial (e)–(h), (i)–(l) [$C_n(\lambda) = \pm 1$] regions of Fig. 5 marked by symbols \star, \diamond, \bullet , respectively. According to Eq. (44) the extremum of Berry curvature occurs close to the points where the exciton band gap is smallest. This naturally happens at \mathbf{K}_\pm unless the splitting is dominated by the DM interaction as discussed below. From the dispersion plots in Fig. 4 it is seen that for a given λ the gaps at \mathbf{K}_\pm are unequal with an inverted order for the opposite λ . This means the main extremum is situated either on \mathbf{K}_- or \mathbf{K}_+ for a given λ . In the trivial case [Figs. 6(a)–6(d)] the (absolute) large Berry curvature values at the extrema are compensated by opposite sign values in the surrounding in the irreducible sector integrating

to zero Chern number. In the nontrivial case [Figs. 6(e)–6(h)] the sign is the same everywhere and the integration leads to Chern numbers ± 1 . Depending on parameters, in particular when DM interaction v_D is large, the minimum gap may shift from \mathbf{K}_\pm to other (C_{3v} equivalent) incommensurate positions closer to the M point in the irreducible BZ sector. Such a case is presented in the Berry curvature plot of Figs. 6(i)–6(l). However, the Chern number is still $C = \pm 1$ since one stays in the nontrivial regime of Fig. 5.

Finally, we comment on the absence of a thermal Hall effect in the present paramagnetic case. The thermal Hall effect has been proposed and investigated many times [30,34,36,58–60] for the FM-ordered honeycomb lattice. In this case time-reversal symmetry is broken and an intrinsic nonzero thermal Hall current carried by the topological magnonic edge states may appear. It vanishes, however, on the antiferromagnetic honeycomb lattice [41] due to the twofold degeneracy of magnon modes caused by a symmetry operation consisting of the product of time reversal and inversion [61]. The situation is similar here in the equivalent sublattice model due to the λ degeneracy of magnetic excitons. But even in the asymmetric case when all modes are split we have the symmetry $\Omega_z(\mathbf{k}, \lambda) = -\Omega_z(-\mathbf{k}, \bar{\lambda})$ which can be seen from Fig. 6. Since the thermal Hall conductivity involves a summation over \mathbf{k}, λ it will vanish also for the most general case of exciton bands which is consistent with the paramagnetic state.

VII. SUMMARY AND CONCLUSION

In this work we have developed a comprehensive theory of paramagnetic excitons on the honeycomb lattice originating from the localized CEF excitations of f -electron elements on the two sublattice sites. We assumed a general case where the inversion symmetry may be broken due to different chemical environment of the sublattices. We focused on a model *without magnetic order* which may be realized for integer J lanthanide ions like Pr, Tm, or U where the CEF ground state can be a nonmagnetic singlet. Specifically, we treated the $J = 4$ based case of an Ising-type singlet-singlet model and an xy -type singlet-doublet model allowed by the C_{3v} site symmetry and with CEF splitting energies $\Delta_{A,B}$. The effective intersite interactions comprise symmetric intrasublattice and intersublattice exchange in both models as well as a new DM-type asymmetric exchange for xy -type model allowed by lack of an inversion center on second-neighbor A - A , B - B bonds. These interactions lead to dispersive magnetic excitons in the paramagnetic state with characteristic properties enforced by the underlying honeycomb symmetry. The dispersion increases with decreasing temperature due to the thermal population effect of CEF levels. We have treated our general model using two alternative techniques, RPA response function method and Bogoliubov bosonic approach, and showed that they lead to equivalent results. The latter approach is the suitable one for discussing topological properties of magnetic excitons.

In the Ising-type case there are two modes which are split by the A, B intersublattice exchange. If inversion symmetry is present, the honeycomb structure enforces the degeneracy of these modes at the zone boundary \mathbf{K}_\pm points. This degeneracy is lifted if the two sublattices become inequivalent

(e.g., have different splittings $\Delta_{A,B}$). For sufficiently strong exchange interactions one mode may turn into a precursor soft mode for an induced magnetic order of the spiral type. The Ising-type model cannot support a DM asymmetric exchange and, therefore, its magnetic excitons are topologically trivial.

This changes in the xy -type singlet-doublet model which supports the DM exchange term. The Fourier transform of the asymmetric exchange is nonvanishing at the \mathbf{K}_{\pm} points. Due to the doublet degeneracy there are now generally four modes present. The symmetric intersite exchange splits them only into two pairs if A, B sublattices are still equivalent, however, even in this case the gap caused by the DM term is preserved at \mathbf{K}_{\pm} . The remaining pair degeneracy is lifted throughout the BZ for sublattice-inequivalent CEF splitting or exchange, except along the ΓM symmetry direction.

In the xy -type model a nonzero DM exchange term exists which has not been considered before in the context of paramagnetic excitons. It may support topologically nontrivial magnetic exciton bands even though there is *no magnetic order* present. This distinguishes the present model from all previous magnetic honeycomb models investigated [36] which all use (anti)ferromagnetic order as a precondition to obtain topological magnon states. We have shown that indeed the nonzero Chern numbers of topological paramagnetic excitons are stable over a wide range of parameter space, in particular for all parameters in the A, B sublattice-equivalent case. The peculiar structure of the underlying Berry curvature in the irreducible BZ sector has been mapped out. Furthermore, we have shown within a continuum approximation for the sublattice-symmetric case that magnetic exciton edge modes inside the 2D bulk magnetic exciton gap caused by DMI at \mathbf{K}_{\pm} exist and their decay length is governed by the ratio of asymmetric DM exchange to symmetric intersublattice exchange. This suggests to extend the present analysis and perform an investigation of edge states of the xy -type magnetic exciton model within a numerical diagonalization approach for various edge and stripe geometries of the honeycomb lattice. Because of the paramagnetic state time-reversal symmetry is not broken and as a consequence these edge modes do not support a thermal Hall effect as another distinction to the magnon topological excitations in the magnetically ordered honeycomb lattice. However, it is possible that, as in the magnetically ordered honeycomb models, a

finite-temperature (pseudospin) Nernst effect [31,41,61] may exist in the paramagnetic exciton case which should be investigated based on the analysis in this work. Furthermore, conduction electrons can easily couple to the gapless edge modes. This will modify their spectral properties which may be accessible by STM investigations.

ACKNOWLEDGMENT

A.A. gratefully acknowledges A. G. Moghaddam for useful discussions.

APPENDIX A: CEF POTENTIAL WITH C_{3v} SYMMETRY, LEVELS, AND EIGENSTATES

Here we discuss to some detail the $J = 4$ CEF states for the less common C_{3v} symmetry of the crystalline electric field potential on the honeycomb lattice because they are, to our knowledge, not easily available in the literature. The corresponding CEF Hamiltonian is given in terms of Stevens operators $O_n^m(\mathbf{J})$ of the ground-state J multiplet which are polynomials of $(n - m)$ th order in J_z and m th order in J_{\pm} according to Refs. [1,2]. Its structure is determined by the symmetry alone but contains six independent CEF potential parameters B_n^m . Formally they may be given in terms of a point-charge model simply representing the neighboring ligands of the f -electron site by Coulomb potentials. The associated charges of the ligands are effective ones screened by the intervening outer-shell (e.g., $5d, 6s$) electrons of f elements [1]. In practice the B_n^m have to be determined from adjustment to experimental quantities like low-temperature specific heat, susceptibility in the whole temperature range, and spectroscopic results from INS or Raman scattering. The C_{3v} CEF Hamiltonian is given by

$$H_{\text{CEF}} = B_2^0 O_2^0 + B_4^0 O_4^0 + B_6^0 O_6^0 + B_4^3 O_4^3 + B_6^3 O_6^3 + B_6^6 O_6^6. \quad (\text{A1})$$

It may be represented as a $(2J + 1) \times (2J + 1)$ matrix in the space spanned by free-ion states $|J, M\rangle$ ($|M| \leq J$). If we rearrange the natural sequence (decreasing M) of $|J, M\rangle$ states suitably H_{CEF} can be written in block-diagonal form according to

$$H_{\text{CEF}} = \begin{pmatrix} & 3 & 0 & -3 & 4 & 1 & -2 & 2 & -1 & -4 \\ 3 & d_3 & m_{30} & m_{33} & 0 & 0 & 0 & 0 & 0 & 0 \\ 0 & m_{30} & d_0 & -m_{30} & 0 & 0 & 0 & 0 & 0 & 0 \\ -3 & m_{33} & -m_{30} & d_3 & 0 & 0 & 0 & 0 & 0 & 0 \\ 4 & 0 & 0 & 0 & d_4 & m_{41} & m_{42} & 0 & 0 & 0 \\ 1 & 0 & 0 & 0 & m_{41} & d_1 & -m_{21} & 0 & 0 & 0 \\ -2 & 0 & 0 & 0 & m_{42} & -m_{21} & d_2 & 0 & 0 & 0 \\ 2 & 0 & 0 & 0 & 0 & 0 & 0 & d_2 & m_{21} & m_{42} \\ -1 & 0 & 0 & 0 & 0 & 0 & 0 & m_{21} & d_1 & -m_{41} \\ -4 & 0 & 0 & 0 & 0 & 0 & 0 & m_{42} & -m_{41} & d_4 \end{pmatrix}, \quad (\text{A2})$$

where the first row and column denote the free-ion M value. In terms of the CEF parameters B_n^m the matrix entries are given by

$$\begin{aligned}
d_4 &= 28[B_2^0 + 30(B_4^0 + 6B_6^0)], \\
d_3 &= 7[B_2^0 - 180(B_4^0 + 17B_6^0)], \\
d_2 &= -8B_2^0 - 660(B_4^0 - 42B_6^0), \\
d_1 &= -17B_2^0 + 180(3B_4^0 + 7B_6^0), \\
d_0 &= -20(B_2^0 - 54B_4^0 + 1260B_6^0), \\
m_{41} &= 15\sqrt{14}(B_4^3 + 24B_6^3), \\
m_{42} &= 720\sqrt{7}B_6^6, \\
m_{30} &= 9\sqrt{35}(B_4^3 - 20B_6^3), \\
m_{33} &= 2520B_6^6, \\
m_{21} &= 15\sqrt{2}(B_4^3 - 42B_6^3). \tag{A3}
\end{aligned}$$

For the eigenvalues and eigenvectors of the three singlets ($\Gamma_{1a,b}, \Gamma_2$) we obtain

$$\begin{aligned}
E_{1a} &= \frac{1}{2}(\beta - \sqrt{8\gamma^2 + \delta^2}), \\
E_{1b} &= \frac{1}{2}(\beta + \sqrt{8\gamma^2 + \delta^2}), \\
E_2 &= \alpha, \tag{A4}
\end{aligned}$$

where we defined

$$\begin{aligned}
\alpha &= d_3 + m_{33}, \\
\beta &= d_0 + d_3 - m_{33}, \\
\gamma &= m_{30}, \\
\delta &= d_0 - (d_3 - m_{33}). \tag{A5}
\end{aligned}$$

According to these expressions the singlet-singlet splitting of the Ising-type $\Gamma_{1a,b}$ model of Sec. III is given by $\Delta = \alpha - \frac{1}{2}(\beta \mp \sqrt{8\gamma^2 + \delta^2})$ and depends, via Eqs. (A3) and (A5), on all six B_n^m CEF parameters. And a similar situation holds for the splitting Δ of the Γ_2 - Γ_3 xy -type singlet-doublet system of Sec. IV.

Furthermore, the corresponding singlet eigenfunctions are given by

$$\begin{aligned}
|\Gamma_{1a}\rangle &= \cos\theta|4, 0\rangle + \sin\theta\frac{1}{\sqrt{2}}(|4, 3\rangle - |4, -3\rangle), \\
|\Gamma_{1b}\rangle &= -\sin\theta|4, 0\rangle + \cos\theta\frac{1}{\sqrt{2}}(|4, 3\rangle - |4, -3\rangle), \\
|\Gamma_2\rangle &= \frac{1}{\sqrt{2}}(|4, 3\rangle + |4, -3\rangle), \\
\cos\theta &= \frac{1}{\sqrt{2}}\sqrt{1 + \frac{1}{\sqrt{1+t^2}}}, \\
\sin\theta &= \frac{1}{\sqrt{2}}\sqrt{1 - \frac{1}{\sqrt{1+t^2}}}, \\
t := \tan(2\theta) &= \frac{2\sqrt{2}\gamma}{\delta}, \quad 0 \leq \theta \leq \frac{\pi}{4}. \tag{A6}
\end{aligned}$$

We note that the *antisymmetric* linear combination of the $|4, \pm 3\rangle$ states belongs to the totally symmetric Γ_1 representation while the symmetric linear combination belongs to Γ_2 .

Because Γ_2 is determined by symmetry alone the eigenvalues and eigenvectors of the remaining singlets $\Gamma_{1a,b}$ are obtained as explicit solutions of a quadratic equation. This factorization of the original 3×3 matrix problem (upper left block in H_{CEF}) is due to the fact that two entries (d_3, d_3) appear pairwise. However, the second and third blocks (which give the twofold-degenerate levels of the three doublets) the equivalent entries (d_2, d_4) are generally different, therefore, the eigenvalues and eigenvectors result from a true cubic equation. It is too tedious and not useful to give their explicit expressions. In the special case when CEF parameters fulfill a constraint such that $d_2 = d_4$ the three doublet eigenvalues will also factorize in one isolated value and a pair resulting from a quadratic equation.

Nevertheless, it is possible to parametrize the form of the doublet eigenfunctions. From the second and third blocks of the matrix representation of H_{CEF} in Eq. (A2) we can read off that they correspond to superpositions like

$$|\Gamma_3^\pm\rangle = u|4, \pm 4\rangle + v|4, \mp 2\rangle \pm w|4, \pm 1\rangle \tag{A7}$$

with normalized coefficients u, v, w which we interpret as coordinates of a point on the surface of a 3D unit sphere spanned by the $|J, \pm M\rangle$ states. Orthonormality is ensured by writing the doublets in the form

$$\begin{aligned}
|\Gamma_{3a}^\pm\rangle &= \sin\chi(\cos\phi|4, \pm 4\rangle + \sin\phi|4, \mp 2\rangle) \\
&\quad \pm \cos\chi|4, \pm 1\rangle, \\
|\Gamma_{3b}^\pm\rangle &= (\cos\alpha\cos\chi\cos\phi - \sin\alpha\sin\phi)|4, \pm 4\rangle \\
&\quad + (\cos\alpha\cos\chi\sin\phi + \sin\alpha\cos\phi)|4, \mp 2\rangle \\
&\quad \mp \cos\alpha\sin\chi|4, \pm 1\rangle, \\
|\Gamma_{3c}^\pm\rangle &= (-\sin\alpha\cos\chi\cos\phi - \cos\alpha\sin\phi)|4, \pm 4\rangle \\
&\quad + (-\sin\alpha\cos\chi\sin\phi + \cos\alpha\cos\phi)|4, \mp 2\rangle \\
&\quad \pm \sin\alpha\sin\chi|4, \pm 1\rangle. \tag{A8}
\end{aligned}$$

The three independent angles χ, ϕ , and α are determined by the three roots of the secular equation of the Hamiltonian doublet block submatrix. The coefficients of the $|\Gamma_{3x}^\pm\rangle$ states turn out to be nothing else than the columns of the Euler-angle parametrization of the 3D rotation matrix, associating $\alpha_{\text{Euler}} \rightarrow \phi$, $\beta_{\text{Euler}} \rightarrow \chi$, $\gamma_{\text{Euler}} \rightarrow \alpha$, and the columns like $1 \rightarrow |\Gamma_{3b}^\pm\rangle$, $2 \rightarrow |\Gamma_{3c}^\pm\rangle$, $3 \rightarrow |\Gamma_{3a}^\pm\rangle$. This holds equivalently with $\beta_{\text{Euler}} \rightarrow \pi - \chi$ for the $|\Gamma_{3x}^\pm\rangle$ states.

APPENDIX B: COLLECTION OF PARAMETERS FOR NUMERICAL CALCULATIONS

We use parameters that absorb the matrix elements m_σ and \tilde{m}_σ of the Ising and xy cases, respectively, into the interaction parameters so that matrix elements do not appear explicitly. This is done by defining the quantities (dimension of energy) v_s, v_2^σ , and v_D^σ ($\sigma = A, B$ sublattice), for brevity we also use

the notation $v_2^{A,B} = v_2(1 \pm \epsilon_2)$ and $v_D^{A,B} = v_2(1 \pm \epsilon_D)$ in the same manner as we have used $\Delta^{A,B} = v_2(1 \pm \epsilon)$ before. Here ϵ , ϵ_2 , and ϵ_D characterize the amount of inversion-symmetry breaking between the sublattices. There are three (five) possible Ising (xy) model parameters given by (coordination numbers $z = 3$, $z_2 = 6$):

Ising-type model:

$$\begin{aligned} v_s &= (m_A m_B I), \\ v_2^\sigma &= (m_\sigma^2 I_2^\sigma), \end{aligned} \quad (\text{B1})$$

leading to

$$\begin{aligned} m_A m_B |I_N(\mathbf{k})| &= (z v_s) |\gamma(\mathbf{k})|, \\ m_\sigma^2 I_D^\sigma(\mathbf{k}) &= (z_2 v_2^\sigma) \gamma_2(\mathbf{k}). \end{aligned} \quad (\text{B2})$$

xy-type model:

$$\begin{aligned} v_s &= (\tilde{m}_A \tilde{m}_B I), \\ v_2^\sigma &= (\tilde{m}_\sigma^2 I_2^\sigma), \\ v_D^\sigma &= (\tilde{m}_D^2 I_D^\sigma), \end{aligned} \quad (\text{B3})$$

leading to

$$\begin{aligned} \tilde{m}_A \tilde{m}_B |I_N(\mathbf{k})| &= |\tilde{I}_N(\mathbf{k})| = (z v_s) |\gamma(\mathbf{k})|, \\ \tilde{m}_A^2 I_D^A(\mathbf{k}\lambda) &= \tilde{I}_D^A(\mathbf{k}\lambda) = (z_2 v_2^A) \gamma_2(\mathbf{k}) + \lambda (z_2 v_D^A) \tilde{\gamma}_D(\mathbf{k}), \\ \tilde{m}_B^2 I_D^B(\mathbf{k}\lambda) &= \tilde{I}_D^B(\mathbf{k}\lambda) = (z_2 v_2^B) \gamma_2(\mathbf{k}) - \lambda (z_2 v_D^B) \tilde{\gamma}_D(\mathbf{k}). \end{aligned} \quad (\text{B4})$$

It is clear that a full consideration of the model in the five-parameter space would be too exhaustive. Therefore, only typical cases will be considered with some sublattice parameters equal and/or some parameters set to zero.

In the definition of the Hamiltonians we choose the convention that positive I, I_2^σ corresponds to FM exchange and negative ones to AF exchange. The same convention applies then to v_s and v_2^σ if we make the reasonable restriction that m_A and m_B matrix elements have the same sign. The sign of I_D^σ is not essential as the DM interaction alternates from bond to bond and from A to B . A change in sign of I_D^σ or v_D^σ just means a redefinition of $\lambda \rightarrow -\lambda$ notation in the exciton bands.

APPENDIX C: RPA RESPONSE FUNCTION APPROACH FOR THE xy -TYPE MODEL

In this model the twofold Γ_3^\pm excited-state degeneracy ($\lambda = \pm$) and two sublattices lead in principle to a 4×4 susceptibility matrix which, however, is the direct sum of 2×2 matrices so that instead of Eq. (6) we now have

$$\begin{aligned} \hat{\chi}(\mathbf{k}, \lambda, i\omega_n) &= [1 - \hat{I}(\mathbf{k}\lambda) \hat{u}(i\omega_n)]^{-1} \hat{u}(i\omega_n), \\ \hat{u}(i\omega_n) &= \begin{pmatrix} u_A(i\omega_n) & 0 \\ 0 & u_B(i\omega_n) \end{pmatrix}, \\ \hat{I}(\mathbf{k}\lambda) &= \begin{pmatrix} I_D^A(\mathbf{k}\lambda) & I_N(\mathbf{k}) \\ I_N^*(\mathbf{k}) & I_D^B(\mathbf{k}\lambda) \end{pmatrix}, \end{aligned} \quad (\text{C1})$$

where the exchange matrix elements are defined in Appendix B above. The single-ion susceptibility (the sum of xx

and yy components) is given by

$$u_\sigma(i\omega_n) = \frac{2\tilde{m}_\sigma^2 \Delta_\sigma P_\sigma(T)}{\Delta_\sigma^2 - (i\omega_n)^2}. \quad (\text{C2})$$

Now the thermal population factor for the singlet-doublet case is $P_\sigma(T) = \tanh \frac{\Delta_\sigma}{2T} (1 + f_\sigma)^{-1}$ where $f_\sigma = \frac{1}{2}(1 - \tanh \frac{\Delta_\sigma}{2T})$. The poles of the dynamical susceptibility associated with magnetic exciton modes may then be obtained in a completely analogous way to the Ising model case, except for the additional mode index λ resulting from the Γ_3 degeneracy:

$$\begin{aligned} \omega_\pm^2(\mathbf{k}\lambda) &= \frac{1}{2} [\omega_A^2(\mathbf{k}\lambda) + \omega_B^2(\mathbf{k}\lambda)] \pm \left[\frac{1}{4} [\omega_A^2(\mathbf{k}\lambda) - \omega_B^2(\mathbf{k}\lambda)]^2 \right. \\ &\quad \left. + 4\tilde{m}_A^2 \tilde{m}_B^2 \Delta_A \Delta_B P_A P_B |I_N(\mathbf{k})|^2 \right]^{\frac{1}{2}}, \\ \omega_\sigma^2(\mathbf{k}\lambda) &= \Delta_\sigma [\Delta_\sigma - 2\tilde{m}_\sigma^2 P_\sigma I_D^\sigma(\mathbf{k}\lambda)]. \end{aligned} \quad (\text{C3})$$

In the zero-temperature limit $P_\sigma \rightarrow 1$ and the above expression is completely equivalent to the xy -model exciton dispersions obtained from the Bogoliubov approach [Eq. (26)]. Likewise, the spectral function of the magnetic response is given in an obvious generalization as

$$S(\mathbf{k}, \omega) = \frac{1}{\pi} \sum_\lambda (\text{Im} \hat{\chi}_{AA}(\mathbf{k}\lambda, \omega) + \text{Im} \hat{\chi}_{BB}(\mathbf{k}\lambda, \omega)). \quad (\text{C4})$$

APPENDIX D: GEOMETRIC PROPERTIES OF HONEYCOMB LATTICE AND BRILLOUIN ZONE

The honeycomb lattice (Fig. 1) has two basis atoms denoted by A and B with a distance d apart (NN distance A - B). The lattice constant is denoted by a (NNN distance A - A or B - B). They are related by $d = a/\sqrt{3}$. We generally use the lattice constant a in the direct lattice and $2\pi/a$ in the reciprocal lattice as units. The three vectors to NN sites δ_i and six vectors to NNN sites $\pm \tilde{\delta}_i$ ($i = 1-3$) are given by

$$\begin{aligned} \delta_1 &= \left(\frac{\sqrt{3}}{6}, \frac{1}{2} \right) a, \quad \delta_2 = \left(\frac{\sqrt{3}}{6}, -\frac{1}{2} \right) a, \quad \delta_3 = \left(-\frac{\sqrt{3}}{3}, 0 \right) a, \\ \tilde{\delta}_1 &= \left(\frac{\sqrt{3}}{2}, \frac{1}{2} \right) a, \quad \tilde{\delta}_2 = \left(-\frac{\sqrt{3}}{2}, \frac{1}{2} \right) a, \quad \tilde{\delta}_3 = (0, -1) a. \end{aligned} \quad (\text{D1})$$

As basis vectors of the unit cell and lattice we may use $\mathbf{v}_1 = -\tilde{\delta}_2$, $\mathbf{v}_2 = \tilde{\delta}_1$. The reciprocal lattice vectors $\mathbf{G}_1, \mathbf{G}_2$ are then defined via $\mathbf{v}_i \cdot \mathbf{G}_j = 2\pi \delta_{ij}$ ($i, j = 1, 2$). Explicitly, we have

$$\begin{aligned} \mathbf{v}_1 &= -\tilde{\delta}_2 = \left(\frac{\sqrt{3}}{2}, -\frac{1}{2} \right) a, \quad \mathbf{v}_2 = \tilde{\delta}_1 = \left(\frac{\sqrt{3}}{2}, \frac{1}{2} \right) a, \\ \mathbf{G}_1 &= \left(\frac{\sqrt{3}}{3}, -1 \right) \frac{2\pi}{a}, \quad \mathbf{G}_2 = \left(\frac{\sqrt{3}}{3}, 1 \right) \frac{2\pi}{a}. \end{aligned} \quad (\text{D2})$$

For the direct unit-cell volume we have $V_c = |\mathbf{v}_1 \times \mathbf{v}_2| = \frac{\sqrt{3}}{2} a^2$ and likewise for the reciprocal cell volume $\Omega_c = |\mathbf{G}_1 \times$

$|\mathbf{G}_2| = \frac{2}{\sqrt{3}}(\frac{2\pi}{a})^2$ which fulfill the relation $V_c \cdot \Omega_c = (2\pi)^2$. The inequivalent zone boundary vectors \mathbf{K}_\pm are given by

$$\begin{aligned}\mathbf{K}_+ &= \frac{1}{3}[\mathbf{G}_1 + 2\mathbf{G}_2] = \left(\frac{\sqrt{3}}{3}, \frac{1}{3}\right) \frac{2\pi}{a}, \\ \mathbf{K}_- &= \frac{1}{3}[2\mathbf{G}_1 + \mathbf{G}_2] = \left(\frac{\sqrt{3}}{3}, -\frac{1}{3}\right) \frac{2\pi}{a}.\end{aligned}\quad (\text{D3})$$

APPENDIX E: PROPERTIES OF MOMENTUM-DEPENDENT HONEYCOMB STRUCTURE FUNCTIONS

The momentum dependence and in particular gap existence of exciton modes at the zone boundary are determined by the structure functions of the nearest- and next-nearest-neighbor

interactions depicted in Fig. 1. They are given by

$$\begin{aligned}\gamma(\mathbf{k}) &= \frac{1}{z} \sum_{\delta} \exp(i\mathbf{k} \cdot \delta), \quad \gamma_2(\mathbf{k}) = \frac{1}{z_2} \sum_{\tilde{\delta}} \exp(i\mathbf{k} \cdot \tilde{\delta}), \\ \gamma_D^{A,B}(\mathbf{k}) &= \frac{1}{z_2} \sum_{\tilde{\delta}} v_{\tilde{\delta}}^{A,B} \exp(i\mathbf{k} \cdot \tilde{\delta}) =: \mp i \tilde{\gamma}_D(\mathbf{k}),\end{aligned}\quad (\text{E1})$$

where $\gamma(\mathbf{k})$ and $\gamma_2(\mathbf{k})$ correspond to the symmetric first (δ) and second ($\tilde{\delta}$) neighbor exchange, with coordination numbers $z = 3$ and $z_2 = 6$, respectively, whereas $\tilde{\gamma}_D(\mathbf{k})$ is associated with the asymmetric DM exchange with second neighbors. The first one is complex with $\gamma(-\mathbf{k}) = \gamma^*(\mathbf{k})$, the second one is real and even $\gamma(-\mathbf{k}) = \gamma(\mathbf{k})$, while the latter is real and odd $\tilde{\gamma}_D(-\mathbf{k}) = -\tilde{\gamma}_D(\mathbf{k})$ under inversion. The latter is due to the staggered nature of the DM interaction leading to $v_{\tilde{\delta}} = -v_{-\tilde{\delta}} = \pm 1$ and $v_{\tilde{\delta}}^B = -v_{\tilde{\delta}}^A$. Explicitly we have, from Fig. 1,

$$\begin{aligned}\gamma(\mathbf{k}) &= \frac{1}{3} \left[\exp i \left(\frac{\sqrt{3}}{6} ak_x + \frac{1}{2} ak_y \right) + \exp i \left(\frac{\sqrt{3}}{6} ak_x - \frac{1}{2} ak_y \right) + \exp \left(-i \frac{\sqrt{3}}{3} ak_x \right) \right], \\ \gamma_2(\mathbf{k}) &= \frac{1}{3} \left[\cos \left(\frac{\sqrt{3}}{2} ak_x + \frac{1}{2} ak_y \right) + \cos \left(-\frac{\sqrt{3}}{2} ak_x + \frac{1}{2} ak_y \right) + \cos ak_y \right], \\ \tilde{\gamma}_D(\mathbf{k}) &= \frac{1}{3} \left[\sin \left(\frac{\sqrt{3}}{2} ak_x + \frac{1}{2} ak_y \right) + \sin \left(-\frac{\sqrt{3}}{2} ak_x + \frac{1}{2} ak_y \right) - \sin ak_y \right].\end{aligned}\quad (\text{E2})$$

It is important to know the behavior of the structure functions around the zone boundary valleys $\mathbf{K}_\pm = (\frac{\sqrt{3}}{3}, \pm \frac{1}{3}) \frac{2\pi}{a}$. We express the momentum by $\mathbf{k} = \mathbf{K}_\pm + \mathbf{q}$ with $|\mathbf{q}| \ll \frac{\pi}{a}$. Then the structure functions in Eq. (E2) may be expanded in terms of \mathbf{q} to lowest order. It is more convenient to use hexagonal coordinates $\mathbf{q}' = (q'_x, q'_y)$ instead of the Cartesian (q_x, q_y) . The transformations between them, for each \mathbf{K}_\pm , are given by

$$\begin{aligned}\mathbf{K}_+ : q'_x &= \frac{1}{2}(\sqrt{3}q_x + q_y), \quad q'_y = -\frac{1}{2}(q_x - \sqrt{3}q_y), \\ \mathbf{K}_- : q'_x &= \frac{1}{2}(\sqrt{3}q_x - q_y), \quad q'_y = \frac{1}{2}(q_x + \sqrt{3}q_y).\end{aligned}\quad (\text{E3})$$

Then the expansion leads to

$$\begin{aligned}\gamma(\mathbf{k}) &= \gamma(\mathbf{K}_\pm + \mathbf{q}') = -\frac{a}{2\sqrt{3}}(q'_x \pm iq'_y), \\ |\gamma(\mathbf{k})|^2 &= \frac{a^2}{12}(q_x^2 + q_y^2) = \frac{a^2}{12}(q'^2_x + q'^2_y) = \frac{\pi^2}{12}\hat{q}^2, \\ \gamma_2(\mathbf{k}) &= \gamma_2(\mathbf{K}_\pm) = -\frac{3}{z_2}, \\ \tilde{\gamma}_D(\mathbf{k}) &= \tilde{\gamma}_D(\mathbf{K}_\pm) = \mp \frac{3\sqrt{2}}{z_2},\end{aligned}\quad (\text{E4})$$

where we defined $\hat{q} = (q_x^2 + q_y^2)^{1/2}/(\pi/a)$. The lowest-order term in $\gamma(\mathbf{k})$ is the term linear in \mathbf{q}' because $\gamma(\mathbf{K}_\pm) = 0$. On the other hand, $\gamma_2(\mathbf{k})$ and $\tilde{\gamma}_D(\mathbf{k})$ have finite values at \mathbf{K}_\pm and no linear terms in \mathbf{q}' . Note that importantly $\tilde{\gamma}_D(\mathbf{K}_\pm)$ changes sign between the nonequivalent BZ boundary points.

APPENDIX F: MOMENTUM GRADIENTS OF STRUCTURE FUNCTIONS AND HAMILTONIAN

The Hamiltonian gradients $\hat{h}_{\mathbf{k}\lambda}^\alpha = \partial \hat{h}_{\mathbf{k}} / \partial k_\alpha$ ($\alpha = x, y$) appearing in the matrix elements for the Berry curvature $\Omega_n^z(\mathbf{k})$ of Eq. (44) are entirely determined by those of the structure functions $\gamma^\alpha(\mathbf{k}) = \partial \gamma(\mathbf{k}) / \partial k_\alpha$ and likewise for $\gamma_2(\mathbf{k})$ and $\tilde{\gamma}_D(\mathbf{k})$. From

Eq. (E2) we get for first neighbors

$$\begin{aligned}\gamma^x(\mathbf{k}) &= i\left(\frac{a\sqrt{3}}{6}\right)\frac{1}{3}\left[\exp i\left(\frac{\sqrt{3}}{6}ak_x + \frac{1}{2}ak_y\right) + \exp i\left(\frac{\sqrt{3}}{6}ak_x - \frac{1}{2}ak_y\right) - 2\exp\left(-i\frac{\sqrt{3}}{3}ak_x\right)\right], \\ \gamma^y(\mathbf{k}) &= i\left(\frac{a}{2}\right)\frac{1}{3}\left[\exp i\left(\frac{\sqrt{3}}{6}ak_x + \frac{1}{2}ak_y\right) - \exp i\left(\frac{\sqrt{3}}{6}ak_x - \frac{1}{2}ak_y\right)\right],\end{aligned}\quad (\text{F1})$$

and for second neighbors

$$\begin{aligned}\gamma_2^x(\mathbf{k}) &= \left(-\frac{\sqrt{3}a}{2}\right)\frac{1}{3}\left[\sin\left(\frac{\sqrt{3}}{2}ak_x + \frac{1}{2}ak_y\right) - \sin\left(-\frac{\sqrt{3}}{2}ak_x + \frac{1}{2}ak_y\right)\right], \\ \gamma_2^y(\mathbf{k}) &= \left(-\frac{a}{2}\right)\frac{1}{3}\left[\sin\left(\frac{\sqrt{3}}{2}ak_x + \frac{1}{2}ak_y\right) + \sin\left(-\frac{\sqrt{3}}{2}ak_x + \frac{1}{2}ak_y\right) + 2\sin(ak_y)\right], \\ \tilde{\gamma}_D^x(\mathbf{k}) &= \left(\frac{\sqrt{3}a}{2}\right)\frac{1}{3}\left[\cos\left(\frac{\sqrt{3}}{2}ak_x + \frac{1}{2}ak_y\right) - \cos\left(-\frac{\sqrt{3}}{2}ak_x + \frac{1}{2}ak_y\right)\right], \\ \tilde{\gamma}_D^y(\mathbf{k}) &= \left(\frac{a}{2}\right)\frac{1}{3}\left[\cos\left(\frac{\sqrt{3}}{2}ak_x + \frac{1}{2}ak_y\right) + \cos\left(-\frac{\sqrt{3}}{2}ak_x + \frac{1}{2}ak_y\right) - 2\cos(ak_y)\right].\end{aligned}\quad (\text{F2})$$

Then, using Eq. (24) we obtain the Hamiltonian gradients as

$$\hat{h}_{\mathbf{k}\lambda}^\alpha = \begin{pmatrix} -\bar{I}_D^{A\alpha}(\mathbf{k}\lambda) & -\bar{I}_N^{\alpha*}(\mathbf{k}) & -\bar{I}_D^{A\alpha}(\mathbf{k}\lambda) & -\bar{I}_N^{\alpha*}(\mathbf{k}) \\ -\bar{I}_N^\alpha(\mathbf{k}) & -\bar{I}_D^{B\alpha}(\mathbf{k}\lambda) & -\bar{I}_N^\alpha(\mathbf{k}) & -\bar{I}_D^{B\alpha}(\mathbf{k}\lambda) \\ \bar{I}_D^{A\alpha}(-\mathbf{k}\bar{\lambda}) & \bar{I}_N^\alpha(-\mathbf{k}) & \bar{I}_D^{A\alpha}(-\mathbf{k}\bar{\lambda}) & \bar{I}_N^\alpha(-\mathbf{k}) \\ \bar{I}_N^{\alpha*}(-\mathbf{k}) & \bar{I}_D^{B\alpha}(-\mathbf{k}\bar{\lambda}) & \bar{I}_N^{\alpha*}(-\mathbf{k}) & \bar{I}_D^{B\alpha}(-\mathbf{k}\bar{\lambda}) \end{pmatrix}, \quad (\text{F3})$$

and the interaction derivatives are obtained from Eq. (25) as

$$\begin{aligned}\bar{I}_D^{A\alpha}(\mathbf{k}\lambda) &= \tilde{m}_A^2 I_D^{A\alpha}(\mathbf{k}\lambda), \\ I_D^{A\alpha}(\mathbf{k}\lambda) &= (z_2 I_2^A) \gamma_2^\alpha(\mathbf{k}) + \lambda (z_2 D_J^A) \tilde{\gamma}_D^\alpha(\mathbf{k}) \\ &= -I_D^{A\alpha}(-\mathbf{k}\bar{\lambda}) = -I_D^{B\alpha}(-\mathbf{k}\lambda), \\ \bar{I}_D^{B\alpha}(\mathbf{k}\lambda) &= \tilde{m}_B^2 I_D^{B\alpha}(\mathbf{k}\lambda), \\ I_D^{B\alpha}(\mathbf{k}\lambda) &= (z_2 I_2^B) \gamma_2^\alpha(\mathbf{k}) - \lambda (z_2 D_J^B) \tilde{\gamma}_D^\alpha(\mathbf{k}) \\ &= -I_D^{B\alpha}(-\mathbf{k}\bar{\lambda}) = -I_D^{A\alpha}(-\mathbf{k}\lambda), \\ \bar{I}_N^\alpha(\mathbf{k}) &= \tilde{m}_A \tilde{m}_B I_N^\alpha(\mathbf{k}), \\ I_N^\alpha(\mathbf{k}) &= (zI) \gamma^\alpha(\mathbf{k}).\end{aligned}\quad (\text{F4})$$

-
- [1] M. T. Hutchings, *Solid State Physics* (Academic, New York, 1964), p. 227.
- [2] K. R. Lea, J. J. M. Leask, and W. P. Wolf, The raising of angular momentum degeneracy of f-electron terms by cubic crystal fields, *J. Phys. Chem. Solids* **23**, 1381 (1962).
- [3] J. Jensen and A. R. Mackintosh, *Rare Earth Magnetism* (Clarendon, Oxford, 1991).
- [4] P. Fulde and I. Peschel, Some crystalline field effects in metals, *Adv. Phys.* **21**, 1 (1972).
- [5] P. Coleman, *Introduction to Many Body Physics* (Cambridge University Press, Cambridge, 2015).
- [6] P. Fulde and M. Loewenhaupt, Magnetic excitations in crystal-field split 4f systems, *Adv. Phys.* **34**, 589 (1985).
- [7] P. Thalmeier and G. Zwicknagl, *Handbook of the Physics and Chemistry of Rare Earths* (Elsevier, Amsterdam, 2005), Chap. 219.
- [8] W. J. L. Buyers, T. M. Holden, and A. Perreault, Temperature dependence of magnetic excitations in singlet-ground-state systems. II. Excited-state spin waves near the Curie temperature in Pr₃Tl, *Phys. Rev. B* **11**, 266 (1975).
- [9] J. G. Houmann, B. D. Rainford, J. Jensen, and A. R. Mackintosh, Magnetic excitations in praseodymium, *Phys. Rev. B* **20**, 1105 (1979).
- [10] Y.-L. Wang and B. R. Cooper, Collective excitations and magnetic ordering in materials with singlet crystal-field ground state, *Phys. Rev.* **172**, 539 (1968).

- [11] Y.-L. Wang and B. R. Cooper, Magnetic ordering in materials with singlet crystal-field ground state. II. Behavior in the ordered state or in an applied field, *Phys. Rev.* **185**, 696 (1969).
- [12] P. Thalmeier, Induced order and collective excitations in three-singlet quantum magnets, *Phys. Rev. B* **103**, 144435 (2021).
- [13] R. J. Birgeneau, E. Bucher, L. Passell, and K. C. Turberfield, Neutron-scattering study of TmSb: A model crystal-field-only metallic paramagnet, *Phys. Rev. B* **4**, 718 (1971).
- [14] R. J. Birgeneau, J. Als-Nielsen, and E. Bucher, Neutron scattering from fcc Pr and Pr₃Tl, *Phys. Rev. B* **6**, 2724 (1972).
- [15] B. R. Cooper, Magnetic excitons in real singlet-ground-state ferromagnets: Application to Pr₃Tl and fcc Pr, *Phys. Rev. B* **6**, 2730 (1972).
- [16] D. B. McWhan, C. Vettier, R. Youngblood, and G. Shirane, Neutron scattering study of pressure-induced antiferromagnetism in PrSb, *Phys. Rev. B* **20**, 4612 (1979).
- [17] R. J. Birgeneau, J. Als-Nielsen, and E. Bucher, Magnetic Excitons in Singlet—Ground-State Ferromagnets, *Phys. Rev. Lett.* **27**, 1530 (1971).
- [18] S. Kawarazaki, Y. Kobashi, M. Sato, and Y. Miyako, Observation of the singlet-singlet crystal-field excitons in PrCu₂ by inelastic neutron scattering, *J. Phys.: Condens. Matter* **7**, 4051 (1995).
- [19] P. S. Savchenkov, E. S. Clementyev, P. A. Alekseev, and V. N. Lazukov, Induced magnetism and “magnetic hole” in singlet ground state system PrNi, *J. Magn. Magn. Mater.* **489**, 165413 (2019).
- [20] T. M. Holden, E. C. Svensson, W. J. L. Buyers, and O. Vogt, Magnetic excitations in terbium antimonide, *Phys. Rev. B* **10**, 3864 (1974).
- [21] P. Thalmeier, Dual model for magnetic excitations and superconductivity in UPd₂Al₃, *Eur. Phys. J. B* **27**, 29 (2002).
- [22] A. Marino, M. Sundermann, D. S. Christovam, A. Amorese, C.-F. Chang, P. Dolmantis, A. H. Said, H. Gretarsson, B. Keimer, M. W. Haverkort, A. V. Andreev, L. Havela, P. Thalmeier, L. H. Tjeng, and A. Severing, Singlet magnetism in intermetallic UGa₂ unveiled by inelastic x-ray scattering, *Phys. Rev. B* (to be published).
- [23] A. Marino, D. S. Christovam, C.-F. Chang, J. Falke, C.-Y. Kuo, C.-N. Wu, M. Sundermann, A. Amorese, H. Gretarsson, E. Lee-Wong, C. Moir, Y. Deng, M. B. Maple, P. Thalmeier, L. H. Tjeng, and A. Severing, Fe substitution in URu₂Si₂: Singlet magnetism in an extended Doniach phase diagram (unpublished).
- [24] H. S. Jeevan, C. Geibel, and Z. Hossain, Quasi-quartet crystal-electric-field ground state with possible quadrupolar ordering in the tetragonal compound YbRu₂Ge₂, *Phys. Rev. B* **73**, 020407(R) (2006).
- [25] T. Takimoto and P. Thalmeier, Theory of induced quadrupolar order in tetragonal YbRu₂Ge₂, *Phys. Rev. B* **77**, 045105 (2008).
- [26] M. J. Daum, A. Ramanathan, A. I. Kolesnikov, S. Calder, M. Mourigal, and H. S. La Pierre, Collective excitations in the tetravalent lanthanide honeycomb antiferromagnet Na₂PrO₃, *Phys. Rev. B* **103**, L121109 (2021).
- [27] H. Ge, C. J. Huang, Q. Zhang, N. Zhao, J. Yang, L. Wang, Y. Fu, L. Zhang, Z. M. Song, T. T. Li, F. Ding, J. B. Xu, Y. F. Zhang, X. Tong, S. M. Wang, J. W. Mei, A. Podlesnyak, L. S. Wu, G. Chen, and J. M. Sheng, Interplay of itinerant electrons and Ising moments in a hybrid honeycomb quantum magnet TmNi₃Al₉, *Phys. Rev. B* **106**, 054434 (2022).
- [28] A. Liu, F. Song, Z. Li, M. Ashtar, Y. Qin, D. Liu, Z. Xia, J. Li, Z. Zhang, W. Tong, H. Guo, and Z. Tian, Ba₉RE₂(SiO₄)₆ (RE=Ho-Yb): A new family of Rare-earth based honeycomb lattice magnets, [arXiv:2305.12214](https://arxiv.org/abs/2305.12214).
- [29] S. A. Owerre, A first theoretical realization of honeycomb topological magnon insulator, *J. Phys.: Condens. Matter* **28**, 386001 (2016).
- [30] S. A. Owerre, Topological honeycomb magnon Hall effect: A calculation of thermal Hall conductivity of magnetic spin excitations, *J. Appl. Phys.* **120**, 043903 (2016).
- [31] S. K. Kim, H. Ochoa, R. Zarzuela, and Y. Tserkovnyak, Realization of the Haldane-Kane-Mele Model in a System of Localized Spins, *Phys. Rev. Lett.* **117**, 227201 (2016).
- [32] H. Kim and S. K. Kim, Topological phase transition in magnon bands in a honeycomb ferromagnet driven by sublattice symmetry breaking, *Phys. Rev. B* **106**, 104430 (2022).
- [33] H. Kondo, Y. Akagi, and H. Katsura, \mathbb{Z}_2 topological invariant for magnon spin Hall systems, *Phys. Rev. B* **99**, 041110(R) (2019).
- [34] E. Aguilera, R. Jaeschke-Ubiergo, N. Vidal-Silva, Luis E. F. Foa Torres, and A. S. Nunez, Topological magnonics in the two-dimensional van der Waals magnet CrI₃, *Phys. Rev. B* **102**, 024409 (2020).
- [35] H. Kondo and Y. Akagi, Dirac Surface States in Magnonic Analogs of Topological Crystalline Insulators, *Phys. Rev. Lett.* **127**, 177201 (2021).
- [36] H. Kondo, Y. Akagi, and H. Katsura, Non-Hermiticity and topological invariants of magnon Bogoliubov–de Gennes systems, *Prog. Theor. Exp. Phys.* **2020**, 12A104 (2020).
- [37] V. Bonbien, F. Zhuo, A. Salimath, O. Ly, A. About, and A. Manchon, Topological aspects of antiferromagnets, *J. Phys. D: Appl. Phys.* **55**, 103002 (2022).
- [38] P. A. McClarty, Topological magnons: a review, *Annu. Rev. Condens. Matter Phys.* **13**, 171 (2022).
- [39] F. Zhuo, J. Kang, A. Manchon, and Z. Cheng, Topological phases in magnonics: A review, [arXiv:2305.14861](https://arxiv.org/abs/2305.14861).
- [40] T. Yu, J. Zou, B. Zeng, J. W. Rao, and K. Xia, Non-Hermitian topological magnonics, [arXiv:2306.04348](https://arxiv.org/abs/2306.04348).
- [41] R. Cheng, S. Okamoto, and D. Xiao, Spin Nernst Effect of Magnons in Collinear Antiferromagnets, *Phys. Rev. Lett.* **117**, 217202 (2016).
- [42] R. P. Madhugaria, S. Mozaffari, H. Zhang, W. R. Meier, S.-H. Do, R. Xue, T. Matsuoka, and D. G. Mandrus, Topological Nernst and topological thermal Hall effect in rare-earth kagome ScMn₆Sn₆, [arXiv:2305.06496](https://arxiv.org/abs/2305.06496).
- [43] M. Matsumoto, B. Normand, T. M. Rice, and M. Sgrist, Field- and pressure-induced magnetic quantum phase transitions in TiCuCl₃, *Phys. Rev. B* **69**, 054423 (2004).
- [44] G. F. Koster, J. O. Dimmock, R. G. Wheeler, and H. Statz, *Properties of the Thirty-two Point Groups* (MIT Press, Cambridge, Massachusetts, 1963).
- [45] P. Y. Portnichenko, A. Akbari, S. E. Nikitin, A. S. Cameron, A. V. Dukhnenko, V. B. Filipov, N. Y. Shitsevalova, P. Čermák, I. Radelytskiy, A. Schneidewind, J. Ollivier, A. Podlesnyak, Z. Huesges, J. Xu, A. Ivanov, Y. Sidis, S. Petit, J.-M. Mignot, P. Thalmeier, and D. S. Inosov, Field-Angle-Resolved Magnetic Excitations as a Probe of Hidden-Order Symmetry in CeB₆, *Phys. Rev. X* **10**, 021010 (2020).

- [46] K. Kudo, T. Takeuchi, H. Ota, Y. Saito, S.-y. Ayukawa, K. Fujimura, and M. Nohara, Superconductivity in hexagonal BaPtAs: SrPtSb- and YPtAs-type structures with ordered honeycomb network, *J. Phys. Soc. Jpn.* **87**, 073708 (2018).
- [47] K. Hanzawa and T. Yamada, Origin of anisotropic RKKY interactions in CeB₆, *J. Phys. Soc. Jpn.* **88**, 124710 (2019).
- [48] T. Yamada and K. Hanzawa, Derivation of RKKY interaction between multipole moments in CeB₆ by the effective Wannier model based on the bandstructure calculation, *J. Phys. Soc. Jpn.* **88**, 084703 (2019).
- [49] B. D. Rainford and J. G. Houmann, Magnetic Exciton Dispersion in Praseodymium, *Phys. Rev. Lett.* **26**, 1254 (1971).
- [50] P. Bak, Theory of paramagnetic singlet-doublet excitations in double-hexagonal close-packed praseodymium, *Phys. Rev. B* **12**, 5203 (1975).
- [51] B. Grover, Dynamical properties of induced-moment systems, *Phys. Rev.* **140**, A1944 (1965).
- [52] P. Thalmeier, Formation of magnetic-biexciton bound states in singlet ground-state systems, *Europhys. Lett.* **28**, 507 (1994).
- [53] K. N. Clausen, K. A. McEwen, J. Jensen, and A. R. Mackintosh, New Mode of Magnetic Excitation in Praseodymium, *Phys. Rev. Lett.* **72**, 3104 (1994).
- [54] T. Moriya, Anisotropic superexchange interaction and weak ferromagnetism, *Phys. Rev.* **120**, 91 (1960).
- [55] Y. Togawa, A. S. Ovchinnikov, and J.-i. Kishine, Generalized Dzyaloshinskii-Moriya interaction and chirality-induced phenomena in chiral crystals, *J. Phys. Soc. Jpn.* **92**, 081006 (2023).
- [56] E. Heinrich, X. Li, and B. Flebus, Spin interactions and topological magnonics in chromium trihalide CrClBrI, *Phys. Rev. B* **104**, 174434 (2021).
- [57] S. Park and B.-J. Yang, Topological magnetoelastic excitations in noncollinear antiferromagnets, *Phys. Rev. B* **99**, 174435 (2019).
- [58] A. Mook, J. Henk, and I. Mertig, Edge states in topological magnon insulators, *Phys. Rev. B* **90**, 024412 (2014).
- [59] K. Fujiwara, S. Kitamura, and T. Morimoto, Thermal Hall responses in frustrated honeycomb spin systems, *Phys. Rev. B* **106**, 035113 (2022).
- [60] P. Czajka, T. Gao, M. Hirschberger, P. Lampen-Kelley, A. Banerjee, N. Quirk, D. G. Mandrus, S. E. Nagler, and N. P. Ong, Planar thermal Hall effect of topological bosons in the Kitaev magnet α -RuCl₃, *Nat. Mater.* **22**, 36 (2023).
- [61] V. A. Zyuzin and A. A. Kovalev, Magnon Spin Nernst Effect in Antiferromagnets, *Phys. Rev. Lett.* **117**, 217203 (2016).